# The accretion history of the Milky Way – II. Internal kinematics of globular clusters and of dwarf galaxies

Francois Hammer, Jianling Wang, Gary A Mamon, Marcel S Pawlowski, Yanbin Yang, Yongjun Jiao, Hefan Li, Piercarlo Bonifacio, Elisabetta Caffau, Haifeng Wang

Monthly Notices of the ROYAL ASTRONOMICAL SOCIETY

MNRAS **527,** 2718–2733 (2024) https://doi.org/10.1093/mnras/stad2922
Advance Access publication 2023 November 20

# The accretion history of the Milky Way – II. Internal kinematics of globular clusters and of dwarf galaxies

Francois Hammer [1]★ Jianling Wang [1,2] Gary A. Mamon [3] Marcel S. Pawlowski,[4] Yanbin Yang [1] Yongjun Jiao,[1] Hefan Li,[2] Piercarlo Bonifacio [1] Elisabetta Caffau[1] and Haifeng Wang[5]

[1]*GEPI, Observatoire de Paris, Paris Sciences et Lettres, CNRS, Place Jules Janssen, F-92195 Meudon, France*
[2]*CAS Key Laboratory of Optical Astronomy, National Astronomical Observatories, Beijing 100101, China*
[3]*Institut d'Astrophysique de Paris (UMR7095: CNRS & Sorbonne Université), 98 bis Bd Arago, F-75014 Paris, France*
[4]*Leibniz-Institut fuer Astrophysik Potsdam (AIP), An der Sternwarte 16, D-14482 Potsdam, Germany*
[5]*CREF, Centro Ricerche Enrico Fermi, Via Panisperna 89A, I-00184, Roma, Italy*

Accepted 2023 September 5. Received 2023 September 1; in original form 2023 July 13

## ABSTRACT

We study how structural properties of globular clusters and dwarf galaxies are linked to their orbits in the Milky Way halo. From the inner to the outer halo, orbital energy increases and stellar-systems gradually move out of internal equilibrium: in the inner halo, high-surface brightness globular clusters are at pseudo-equilibrium, while further away, low-surface brightness clusters and dwarfs appear more tidally disturbed. Dwarf galaxies are the latest to arrive into the halo as indicated by their large orbital energies and pericentres, and have no time for more than one orbit. Their (gas-rich) progenitors likely lost their gas during their recent arrival in the Galactic halo. If dwarfs are at equilibrium with their dark matter (DM) content, the DM density should anticorrelate with pericentre. However, the transformation of DM dominated dwarfs from gas-rich rotation-supported into gas-poor dispersion-supported systems is unlikely accomplished during a single orbit. We suggest instead that the above anticorrelation is brought by the combination of ram-pressure stripping and of Galactic tidal shocks. Recent gas removal leads to an expansion of their stellar content caused by the associated gravity loss, making them sufficiently fragile to be transformed near pericentre passage. Out of equilibrium dwarfs would explain the observed anticorrelation of kinematics-based DM density with pericentre without invoking DM density itself, questioning its previous estimates. Ram-pressure stripping and tidal shocks may contribute to the dwarf velocity dispersion excess. It predicts the presence of numerous stars in their outskirts and a few young stars in their cores.

**Key words:** Galaxy: halo – globular clusters: general – galaxies: dwarf – Galaxy: evolution – galaxies: interactions.

## 1 INTRODUCTION

Milky Way (MW) globular clusters (GCs) and dwarf galaxies are unique systems, because they are sufficiently close to allow estimating their intrinsic properties on one hand, and their 3D bulk motions thanks to the combination of redshifts and proper motions (PMs). Considerable efforts have been made in estimating their structural (Muñoz et al. 2018, and references therein), kinematic (Simon 2019, and references therein), and orbital (Li et al. 2021; Hammer et al. 2023) properties. We have recently shown that GC half-light radii are inversely proportional to their bulk orbital energies, and therefore mostly determined by MW tides, which impact depends strongly on the number of pericentre passages (Hammer et al. 2023, hereafter Paper I).

The main intrinsic properties of GCs and dwarf galaxies are their half-light radii ($r_{\rm half}$).[1], their velocity dispersion ($\sigma_{\rm los}$ and for some GCs, $\sigma_{\rm pm}$ from PMs), and their total $V$-band luminosities ($L_V$). The main orbital properties are the total energy, the angular momentum, the pericentre and the eccentricity of their orbits. Here, we consider the correlations between structural and orbital properties of both GCs and dwarfs to investigate how their host affects them. As in Paper I, we consider all stellar systems of the MW halo, that is, GCs and dwarf galaxies. Our motivation is two-fold: first, these systems have a similar range in stellar mass, and second, as pointed out by Marchi-Lasch et al. (2019), there are similarities between structural properties of ultra-faint dwarfs (UFDs) and low surface brightness GCs. This leads us to distinguish three categories of populations, the high-surface brightness (HSB-GCs, with $\log(SB/L_\odot pc^{-2} > 2)$, the low-surface brightness (LSB-GCs, with $\log(SB/L_\odot pc^{-2} < 2)$ GCs (see fig. 1 of Paper I, where SB is defined as the mean surface-brightness within the half-light radius), and the dwarf galaxies with lower surface brightness than that of LSB-GCs.

Paper I has also established an empirical relation between the infall lookback time and the logarithm of the orbital energy, for which the time has been calibrated from the age of GCs associated to the different merger events that occurred in the MW (Kruijssen et al. 2019, 2020; Malhan et al. 2022). This empirical relation is in

★ E-mail: francois.hammer@obspm.fr

[1] $r_{\rm half}$ is the half-projected-light radius, which is usually called *effective radius*, though we kept the first appellation for consistency with Paper I.

excellent agreement with theoretical predictions from cosmological simulations[2] (Rocha, Peter & Bullock 2012). It suggests that most dwarfs arrived recently ($< 3$ Gyr) in the MW halo, because, for example their orbital energy is larger than that of Sgr, which is known to have been accreted $5 \pm 1$ Gyr ago. Such a recent arrival for dwarfs could have a considerable impact on their past evolution and even on their dark matter (DM) content. During such a small elapsed time, dwarf orbiting at large distances and with large pericentres (such as those of classical dwarfs but Sgr) would not make more than one orbit. Because their progenitors far from the MW halo have to be gas-rich dwarfs (Grcevich & Putman 2009) dominated by rotation, their properties may be governed by their gas losses during their infall into the MW halo. This mechanism has been studied intensively and proved to be effective by Mayer et al. (2006) for DM dominated progenitors, assuming the transformation was done in a Hubble time-scale. Here, dwarf progenitors would have much less time to be transformed into dispersion supported dwarfs, so their DM content should be more limited than what was assumed by Mayer et al. (2006).

Section 2 describes the orbital and intrinsic properties of samples of GCs and of dwarf galaxies, and Section 2.4 discusses how dwarf eccentricities and infall times depends on the MW total mass. Section 3 compares the intrinsic GC properties, and how they correlate[3] with orbital properties, showing that HSB-GCs are in pseudo-equilibrium with MW tides, while LSB-GCs appear to be much less in equilibrium. For dwarf galaxies, Section 4 presents a strong correlation between a simple combination of intrinsic parameters ($\sigma^2_{\rm los}/r_{\rm half}$) and the pericentre, which is at the origin of many correlations shown throughout the Paper. Section 5 shows that these correlations can be explained if recently infalling dwarfs have been stripped of their gas and tidally shocked by the MW. It also provides a theoretical calculation for the effect, which is confirmed by numerical simulations (Section 5.2). It leads to important predictions, for example of a tiny young stellar component in their cores (Section 5.4), of the presence of a stellar halo surrounding most MW dwarfs (Section 5.5), and on some limitations about the DM content of MW dwarfs (Section 5.7). Section 6 summarizes the results and conclusions of this study.

## 2 ORBITAL AND INTRINSIC PROPERTIES OF GCS AND DWARFS

### 2.1 GCs

In the following, we consider the data for 156 GCs from Baumgardt (2017); Sollima & Baumgardt (2017); Baumgardt & Hilker (2018); Baumgardt, Sollima & Hilker (2020); Baumgardt & Vasiliev (2021), which include their intrinsic parameters such as half-light radii and velocity dispersions. PMs from *Gaia* EDR3 are taken from Vasiliev & Baumgardt (2021). Tables A1 and A2 in Appendix of Paper I provide the resulting orbital parameters (velocities and orbital radii) and their error bars for a MW model following Eilers et al. (2019, see also a more detailed description in Jiao et al. 2021).

[2]However a very different analysis (Barmentloo & Cautun 2023) has been recently published, which is discussed in Appendix A.

[3]Throughout the manuscript we have used a Spearman's rank correlation $\rho$ that does not assume any shape for the relationship between variables; the significance and associated probability of $\rho$ have been tested using $t = \rho\sqrt{(n-2)/(1-\rho^2)}$, which is distributed approximately as Student's $t$ distribution with $n-2$ degrees of freedom under the null hypothesis.

**Table 1.** Properties of the four MW DM mass models to be associated to the baryonic discs and bulge (see text).

| Quantity (units) | Einasto$_{\rm HM}$ | NFW | Einasto$_{\rm MM}$ | Einasto$_{\rm LM}$ |
|---|---|---|---|---|
| $M_{\rm DM}$ ($10^{11}$ M$_\odot$) | 14.1 | 7.2 | 4.2 | 1.9 |
| $M_{\rm tot}$ ($10^{11}$ M$_\odot$) | 15 | 8.1 | 5.1 | 2.8 |
| $r_{200}$ (kpc) | 236 | 189 | 164 | 135 |
| $r_{-2}$ (kpc) | 29.89 | 14.80 | 12.81 | 9.73 |
| Einasto index | 6.33 | – | 3.00 | 1.67 |
| $\chi^2_\nu$ | 1.57 | 1.27 | 1.21 | 0.72 |

*Note.* $M_{\rm DM}$ and $M_{\rm tot}$ are defined within the virial radius $r_{200}$. $r_{-2}$ is the radius where the logarithmic slope of the density profile is equal to $-2$ for direct comparison between the NFW and Einasto profiles. The last row ($\chi^2_\nu$) provides their goodnesses in fitting the MW rotation curve (see calculation details in Jiao et al. 2021)

### 2.2 Dwarf galaxies

For dwarf galaxies, we are using the data from *Gaia* EDR3 (Li et al. 2021, see their Tables for each MW mass models) using the same prescriptions as for GCs for deriving orbital parameters. Appendix B describes the adopted values for dwarf intrinsic parameters, and their references (see Table B1).

### 2.3 Sample definition

Since the goal of this series of papers is to examine the impact of the MW on its halo inhabitants, we have not considered GCs that are associated to the LMC. The same applies for dwarf galaxies and we have excluded Carina II, Carina III, Phoenix II, Horologium I, Hydrus I, and Reticulum II, which are associated to the LMC on the basis of their relative PMs (Erkal & Belokurov 2020; Patel et al. 2020). This reduces the potential impact of a massive LMC, which has not been considered in the following. This leaves us with 26 dwarf galaxies having measurements of their internal kinematics ($\sigma_{\rm los}$), to which we may add Sgr, the status of which is quite special given its large system of tidal tails (Ibata et al. 2001). In the following we will only consider the sample of 26 MW dwarfs, without Sgr (see table B1 of Appendix B).

### 2.4 MW mass models and how they affect GC and dwarf orbits

Eilers et al. (2019) modelled the MW rotation curve using a mass model that includes a bulge, a thick and a thin disc following Pouliasis, Matteo & Haywood (2017) corresponding to a total baryonic mass of $0.89 \times 10^{11} M_\odot$, and a halo DM component. Here, the halo is represented by four different models. The first one is a NFW model (Navarro, Frenk & White 1996) that requires a cut-off radius fixed at $R_{\rm vir} = 189$ kpc to avoid infinite mass (see details in Paper I), and for consistency with orbital calculations tabulated in Li et al. (2021) and in Paper I. This model is very similar than the fiducial *MWPotential14* from Bovy (2015) which has been widely used. We are also considering the whole range of MW mass models able to fit the rotation curve (see, e.g. Jiao et al. 2021), by considering three different Einasto (Einasto 1965, see Table 1 and also Retana-Montenegro et al. 2012) profiles, which include the largest and smallest MW mass (model high and low mass, HM and LM, respectively) and a median mass (MM, see Table 1). Einasto$_{\rm HM}$ model shares a similar total mass than the McMillan (2017) model, while conversely to the later, it is consistent with the MW rotation curve from Eilers et al. (2019). Einasto$_{\rm MM}$ model is coming from the analysis of MW rotation curves and GCs made by Wang, Hammer & Yang (2022). Einasto$_{\rm LM}$ is rather similar (but with a slightly higher

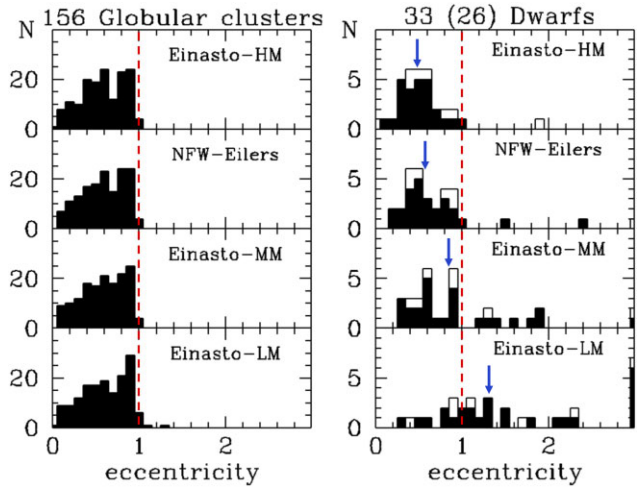


**Figure 1.** Histograms of the eccentricity distribution of GCs (*left*) and dwarf galaxies (*right*) for four MW mass models (decreasing total mass from top to bottom) that are consistent with the MW rotation curve (Jiao et al. 2021). *Open* and *filled histograms* represent all the 33 dwarfs, and a subsample of 26 of them having their internal velocity dispersion measured. The *blue arrows* in the right panels indicate the median eccentricities of 0.478, 0.581, 0.829, and 1.301 from the top to the bottom. The *vertical red-dashed line* delimits eccentricity = 1.I have

total mass) to that of Ou et al. (2023) who generated the first Einasto modelling based on the MW rotation curve obtained from *Gaia* EDR3.

For each MW mass model, GC and dwarf eccentricities are calculated from GALPY (Bovy 2015) using Monte Carlo realizations. For elliptical orbits the eccentricity is

$$\mathrm{ecc} = \frac{R_{\mathrm{apo}} - R_{\mathrm{peri}}}{R_{\mathrm{apo}} + R_{\mathrm{peri}}} . \quad (1)$$

For hyperbolic orbits, we estimated the eccentricity after deriving the angle $2\theta$ between asymptotes

$$\mathrm{ecc} = -\frac{1}{\cos(\theta)} . \quad (2)$$

Fig. 1 shows how the orbital eccentricity depends on the MW mass models. The distribution of eccentricities of 156 GCs is very stable when decreasing the MW mass from 15 to $5.1 \times 10^{11}$ $M_\odot$, that is, all of them follow elliptical and bound orbits. It is only by adopting the smallest MW mass ($2.8 \times 10^{11}$ $M_\odot$) that the Pyxis and Terzan 8 orbits becomes hyperbolic (eccentricity = 1.3 and 1.07, respectively), while the orbits of three other GCs (Pal 3, Eridanus, and Arp 2) have eccentricities just below 1.

This contrasts with the net increase of dwarf eccentricities when the MW mass decreases, from the top to the bottom right panels of Fig. 1. Dwarf galaxies show a smaller median eccentricity than that of GCs for high MW mass models, while two-thirds of them are on hyperbolic orbits for the lowest MW mass model (Einasto$_{\mathrm{LM}}$). Table B2 of Appendix B gives dwarf eccentricities for each of the four adopted MW mass models of Table 1.

Fig. 1 illustrates that by using GCs to characterize the MW mass, one would find values close or larger than that of the Einasto-MM model (e.g. see Wang et al. 2022 and references therein). If considering dwarfs as MW satellites, one would automatically derive large masses for the MW, which suggests that MW mass determinations are strongly affected by the choice of adopted priors. It implies that the total dynamical mass of the MW derived from the *Gaia* DR2 rotation curve (Eilers et al. 2019; Jiao et al. 2021) is still an unknown within a large range of values.

Another illustration of the impact of the MW mass choice is given by the determinations of the infall time for MW dwarfs. According to Boylan-Kolchin et al. (2013), satellites with the most recent infall have the largest orbital energy (or the smallest binding energy), which is well illustrated in fig. 1 of Rocha et al. (2012). This follows the expectations of the *onion skin* model of Gott (1975). It has prompted many studies (Rocha et al. 2012; Fillingham et al. 2019; Miyoshi & Chiba 2020; Barmentloo & Cautun 2023) to use dedicated zoomed simulations to directly compare MW dwarfs with simulated satellites. If considering large MW masses, dwarf galaxies would have smaller energy than objects near the escape velocity lines, which unavoidably leads to large infall lookback times, as found by the above studies that considered $M_{\mathrm{tot}}/(10^{11}\ M_\odot) = 19$, 10–25 (average 17 from the ELVIS suite, Garrison-Kimmel et al. 2014), 15.4, and 10–20, respectively. Right panels of Fig. 1 show that by decreasing the MW mass below this range, more and more dwarfs become unbound, leading to small infall lookback times. It suggests that the inferred infall time is thus dependent on what total MW mass has been assumed.

This is why, in Paper I and in this paper, we have adopted a different approach by estimating only relative infall times, after comparing MW dwarf orbital energies to robust estimates of the infall times for past merger events in the MW (Kruijssen et al. 2020; Malhan et al. 2022), that is, independently of the MW mass. Our constraints on the MW dwarf infall time are coming from a comparison with assumed *Gaia*-Sausage-Enceladus (8–10 Gyr ago) and Sgr (4–6 Gyr ago) infall times. Since the orbital energy of MW dwarfs are larger than that of the latter events, their infall epochs are expected to be more recent (see fig. 6 of Paper I).

In the following section, we will try to identify which relationship between intrinsic and orbital properties is independent on the MW mass model, either for dwarfs or for GCs.

## 3 GC PROPERTIES

### 3.1 The correlation between half-light radius, pericentre radius, and total energy

In Paper I, we have shown that the half-light radius scales as the inverse of the total orbital energy ($E_{\mathrm{tot}}$) for the NFW model of the MW (Eilers et al. 2019; Jiao et al. 2021, see also Table 1). Fig. 2 illustrates that this anticorrelation trend is highly significant (probability of a coincidence smaller than $10^{-20}$). We have tested the slope of the logarithmic relation between $r_{\mathrm{half}}$ and $E_{\mathrm{tot}}$ for the 4 MW mass models of Table 1, which ranges from –1.1 ± 0.3 to –1.18 ± 0.3. We then adopt[4] −1 for simplicity, that is, $E_{\mathrm{tot}} \propto 1/r_{\mathrm{half}}$ in Fig. 2. It shows that the GC size depends on the number of previous passages at pericentre, and that smaller stellar systems are associated to early infall into the MW (see Paper I). This relation does not depend on the MW model as it is illustrated by comparing top and bottom panels of Fig. 2, for which GCs share very similar locations. Fig. 2 also illustrates how identified structures (see coloured points) have almost a single energy value, suggesting the relation between their formation epoch and the energy described in Paper I.

For GCs we adopt the same relation as Baumgardt (2017) between the dynamical mass (or total mass inside $r_{\mathrm{half}}$) and the velocity

[4]Slopes (a) provided in the top-right side of each panel of Fig. 2 are coming from the linear fit of $E_{\mathrm{tot}}$ with $1/r_{\mathrm{half}}$, and are then different that those from the logarithmic relation.

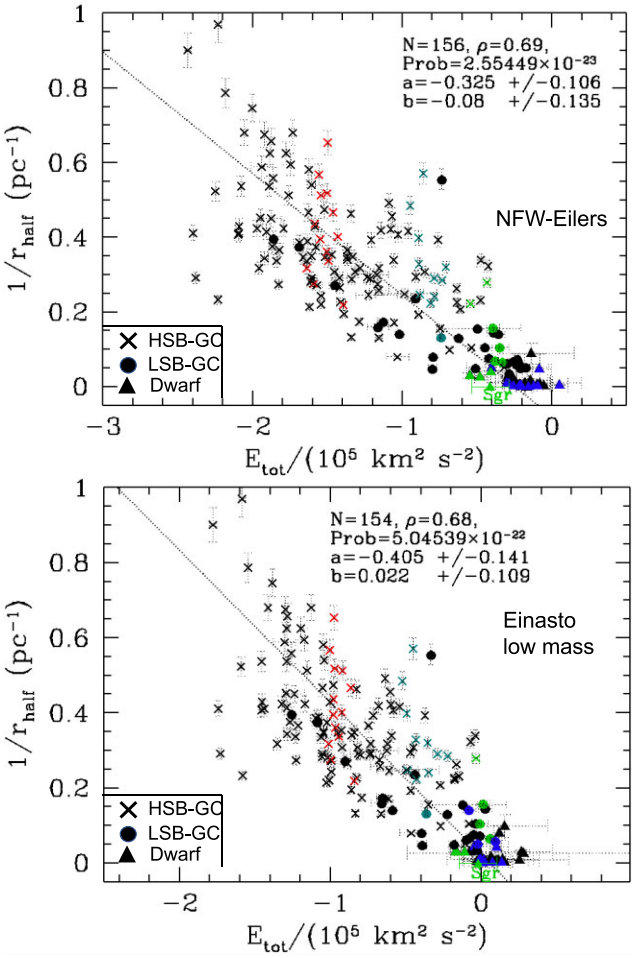


**Figure 2.** Inverse of the half-light radius versus total orbital energy, for HSB-GCs (*crosses*), LSB-GCs (*full dots*), and dwarfs (*triangles*). Identified structures by Malhan et al. 2022 and Kruijssen et al. 2020 are represented by different colour codes (Kraken: red; *Gaia*-Sausage-Enceladus: cyan; Sgr: green). Dwarf galaxies and LSB-GCs belonging to the VPOS (Pawlowski, Pflamm-Altenburg & Kroupa 2012) are shown with blue colours. The *top* (*bottom*) panel shows 156 (154) GCs and 33 dwarfs after calculating the total energy from the NFW (Einasto-low mass) model of the MW. The location of Sgr is indicated by a *green triangle*. The *dotted line* shows the fit of the GC points, and the corresponding slope (a) and rest (b), as well as the significance of the Spearman rank correlation are given on the top-right of each panel. One sigma error bars on orbital quantities such as pericentre and total energy are based on Monte Carlo calculations assuming Gaussian distributions for PM and radial velocity errors.

dispersion and the half-light radius, which has been established by Wolf et al. (2010), under the assumption of self-equilibrium and constant line-of-sight velocity dispersion:

$$\frac{M_{\rm tot}(r_{\rm half})}{1\,{\rm M}_\odot} = 930 \left(\frac{\sigma_{\rm los}}{1\,{\rm km\,s^{-1}}}\right)^2 \left(\frac{r_{\rm half}}{1{\rm pc}}\right) , \quad (3)$$

where $\sigma_{\rm los}$ has been estimated within $r_{\rm half}$.

By dividing the total mass by $r^2_{\rm half}$ and by $r^3_{\rm half}$, one obtains quantities proportional to the averaged surface density $\Sigma_{\rm tot} \propto \sigma^2_{\rm los}/r_{\rm half}$ and to the 3D density ($\rho_{\rm tot} \propto \sigma^2_{\rm los}/r^2_{\rm half}$) inside $r_{\rm half}$, respectively. Fig. 3 shows how the two latter quantities depend on pericentre[5]

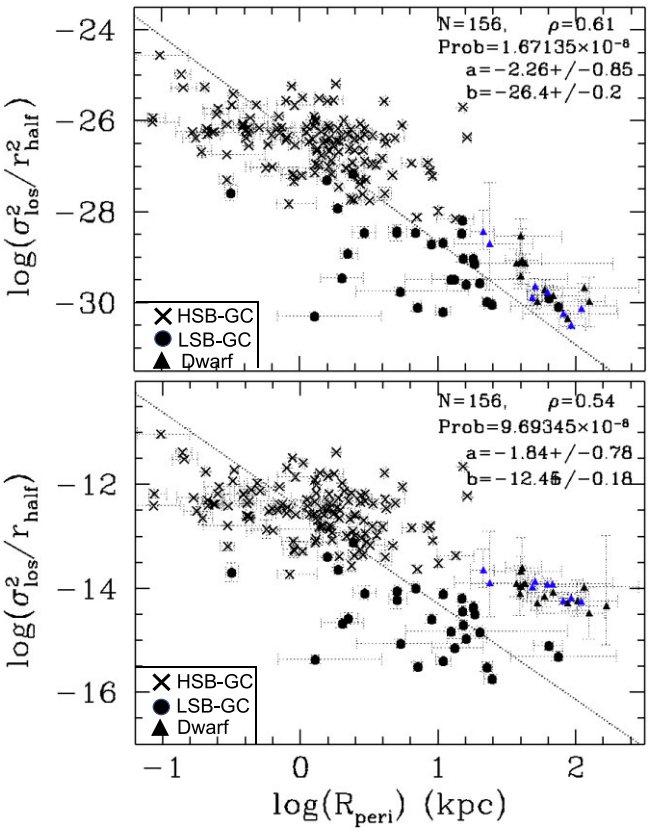


**Figure 3.** $\sigma^2_{\rm los} r^2_{\rm half}$ (proportional to a 3D density) and $\sigma^2_{\rm los} r_{\rm half}$ (proportional to a surface density) of GCs versus $R_{\rm peri}$. Same symbols than for Fig. 2, except that here only VPOS dwarfs have kept their (blue) colour. One sigma error bars on orbital quantities such as pericentre and total energy are based on Monte Carlo calculations assuming Gaussian distributions for PM and radial velocity errors.

The resulting anticorrelations (see straight-dotted lines) are not unexpected for GCs. We have shown that their pericentre (and angular momentum) is well correlated with their energy (see Paper I), while Fig. 2 shows how the energy correlates with the half-light radius. The latter correlation is likely responsible for the strong, but quite scattered relation between surface-density and 3D-density with pericentre.

Fig. 4 shows how slope, correlation significance, and probability are changing with X when considering the relation between $\sigma^2_{\rm los}\, r^X_{\rm half}$ and $R_{\rm peri}$ for 156 GCs. For $X = 1$, the former represents the total mass that barely correlates with $R_{\rm peri}$, while the anticorrelation coefficient ($\rho$) increases for increasing $|X|$. This is expected because the pericentre should be directly related to the orbital energy (see Paper I), which is proportional to the half-mass radius (see Fig. 2), so the velocity dispersion should be a more minor factor.

### 3.2 How tidal shocks affect an orbiting stellar system

Tidal shocks exerted on GCs near their pericentre have been theoretically described for orbits passing close to the bulge or through the disc (Aguilar et al. 1988; Gnedin & Ostriker 1999). Aguilar et al. (1988) showed that the average energy increase of a star after

[5]Here we choose to use pericentre instead of the total orbital energy since we need to establish logarithmic relations to identify their scaling power; one may recall that many dwarfs and even few GCs can be unbound and with positive energy, contrary to most inhabitants of the MW halo (see Fig. 1).

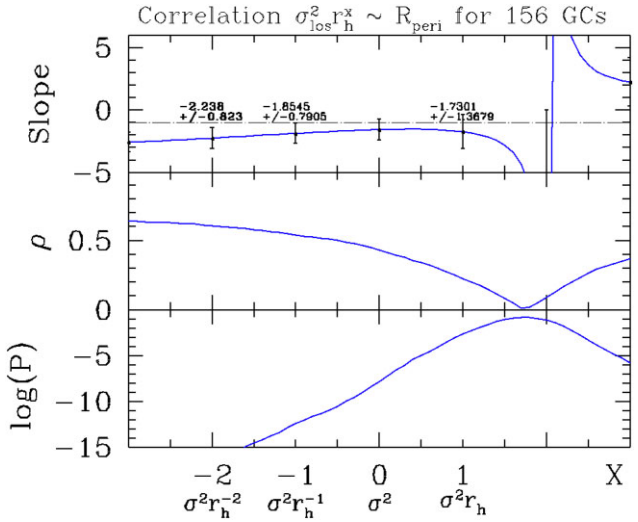


**Figure 4.** Slope, correlation $\rho$ (its absolute value), and associated probability (in logarithmic scale) of the correlation between $\sigma^2_{los} r^X_{half}$ and $R_{peri}$ for $X$ (in abscissa) taking values from $-3$ to $+3$. Each quantity is shown on the $X$ axis. The NFW model has been assumed for calculating $R_{peri}$, but curves for other models cannot be distinguished from it.

integrating over the whole GC has been calculated to be

$$\Delta E = \frac{4}{3}\,\eta \left(\frac{G M_{MW}(R_{peri})}{R^2_{peri}}\right)^2 \left(\frac{r_{rms}}{V_{peri}}\right)^2, \quad (4)$$

where $V_{peri}$ is the velocity at pericentre, $\eta$ is a dimensionless parameter that accounts for our lack of understanding of the details of the tide (deviations from the impulsive approximation[6]), and

$$r^2_{rms} = 3\, r^2_{half,3D}, \quad (5)$$

with

$$r_{half,3D} = \frac{4}{3} r_{half}, \quad (6)$$

the latter comes from Wolf et al. (2010) after transforming the theoretical $r_{half,\,3D}$ into the observed $r_{half}$ calculated from the stellar surface density. The problem with the rms radius is that it may diverge for models whose outer density slope is $>-5$ (including the Plummer model, often used to represent the density profiles of GCs). Only the King (1966) model and truncated models would have finite rms radius. One possibility is to limit the calculation of the rms radius to the bound particles.

One extreme case is tidal disruption, where, to first order, the energy impulse per unit mass from the MW tide matches the binding energy per unit mass $3/2\sigma^2$, where $\sigma$ is the average one-dimensional velocity dispersion of the system (but see van den Bosch et al. 2018 for a more detailed analysis that shows the resilience of stellar systems to tides). Then, one can combine equations (4), (5), and (6), yielding

$$\frac{\sigma^2}{r^2_{half}} = \frac{128}{27}\,\eta \left(\frac{g_{MW}(R_{peri})}{V_{peri}}\right)^2, \quad (7)$$

where $g_{MW}(R_{peri}) = G M_{MW}(R_{peri})/R^2_{peri}$ is the gravitational acceleration exerted by the assumed spherical MW at $R_{peri}$. Values

[6] $\eta$ is always equal or less than 1, except in the outermost layers of the satellite due to resonances. It absorbs the effects of adiabatic invariants, and of an extended perturber (the impulse approximation involves a point-like perturber). Both effects shrink the magnitude of the effect of the tidal shock.

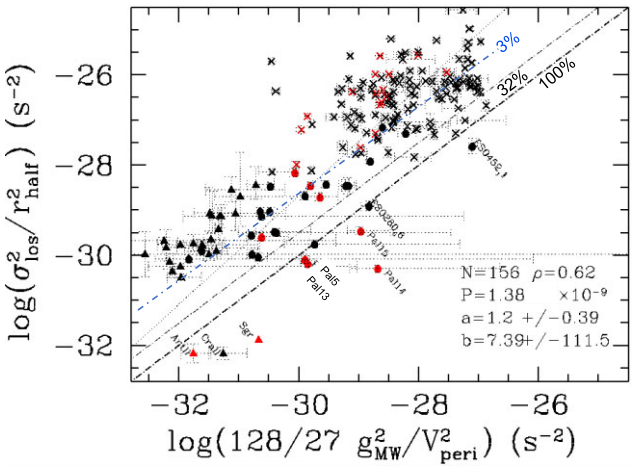


**Figure 5.** Correlation between internal GC properties ($\sigma^2_{los} r^2_{half}$, proportional to 3D density) and external properties from tidal shock theory for a GC (Aguilar, Hut & Ostriker 1988; Gnedin & Ostriker 1999) passing near pericentre to be disrupted (see equation (8)). Same symbols as in Fig. 2, but now indicating in red colour the GCs associated to a tidal tail (Zhang, Mackey & Da Costa 2022, see their Table 3). *Dot-dashed lines* correspond to the equality, $f = 1$ (*thick*), to $f = 0.32$ (*thin*), and to $f = 0.032$ (*blue*), respectively, the latter being almost confused with the *dotted line* that represents the correlation for GCs. All quantities in the abscissa have been extracted at $R_{peri}$.

of $g_{MW}$ and of $V_{peri}$ have been derived from Monte Carlo realizations assuming Gaussian distributions for PM and radial velocity errors. These calculations are based on GALPY (Bovy 2015), to warrant a correct propagation of errors as well as to consider effects related to axisymmetric discs. However, equation (7) corresponds to the specific and extreme case when the energy impulse per unit mass equals the binding energy per unit mass. In the following, we generalize it by considering cases for which the energy impulse only amounts to a fraction $f$ of the binding energy, which applies to many systems that can be affected by tides, but not fully destroyed by them. To simplify, $f$ also accounts for $\eta$, and the latter can shrink below 1 (see fig. 3 of Aguilar et al. 1988). This leads to

$$\frac{\sigma^2}{r^2_{half}} \times f = \frac{128}{27} \left(\frac{g_{MW}(R_{peri})}{V_{peri}}\right)^2. \quad (8)$$

Equation (8) compares structural (left) with orbital (right) quantities, which is illustrated in Fig. 5, in which we have assumed $\sigma = \sigma_{los}$ in spherical symmetry, a condition that is verified for most GCs. Equation (8) accounts for bulge and disc shocks, which are both described by the same formulae, though with different time-scales.

The left hand of equation (8) corresponds to the square of the inverse crossing time

$$t_{cross} = \frac{r_{half}}{\sigma} \quad (9)$$

for a star inside a stellar system, while the right hand estimates the inverse-square of a time ($t_{perturber}$) linked to the perturber passage[7], that is, the MW. In the case of a fast perturber, $t_{shocks} \leq t_{cross}$

[7] The tidal shock time is $t_{shock} = R_{peri}/V_{peri}$, which is equal to $t_{perturber} \times (GM_{MW}/R_{peri})/(0.459 V^2_{peri})$, that is, their ratio is that coming from both sides of the virial theorem, $0.5 V^2_{peri} = GM_{MW}/R_{peri}$. If the system is fully virialized the ratio should be very close to 1, though even when not at equilibrium it could not be very different than 1.

and the impulse approximation may apply (Aguilar & White 1985; Gnedin & Ostriker 1997), implying that stellar systems found below the equality line in Fig. 5 are likely tidally shocked, disrupted, or stripped. In such a case, the energy brought by tidal shocks becomes equal or larger than the kinetic energy necessary to balance the self-gravity of the stellar system, which becomes dominated by tides.

One would expect that such stellar systems may show tidal tails. Red symbols in Fig. 5 indicate GCs for which such tail systems have been identified (Ibata et al. 2021; Zhang et al. 2022, see their table 3), although these surveys cannot be considered as complete since not all GCs have been scrutinized for tidal tail search.

### 3.3 The different properties of HSB and of LSB-GCs

Fig. 5 reveals large differences when comparing HSB with LSB-GCs. HSB-GCs appear much more robust against tides, since none (among 127) are below the equality line $f = 100$ per cent. It contrasts with the 7 (24 per cent) LSB-GCs that lie well below the line. Most of the latter possess a known system of tidal tails (4 among 7), while tails are less frequent for LSB-GCs above the line (4 among 22). This furthermore contrasts with HSB-GCs, for which all systems possessing tidal tails are well above the equality line, and even above the $f = 0.32$ line.

Fig. 5 shows that quantities at both sides of equation (8) correlate well (156 GCs, $\rho = 0.62$, $P = 1.4 \times 10^{-9}$). Here we show that it is due to the fact that both quantities anticorrelate with the pericentre. According to the top panel of Fig. 3, $\sigma^2_{\rm los}/r^2_{\rm half}$ evolve as $R^{-2.26}_{\rm peri}$. Most HSB-GCs have their orbits within 15 kpc, for which $M_{\rm MW} \propto$ R (see, e.g. Jiao et al. 2021), and then $g_{\rm MW} = GM_{\rm MW}/R^2 \propto R^{-1}$, and we also find (see Appendix C) that $V_{\rm peri}$ is almost independent to $R_{\rm peri}$. It lets the second hand of equation (8) following to $R^{-2}_{\rm peri}$. In other words, stellar systems have decreasing pericentre, orbital energy, and half light radii from the left to the right of Fig. 5.

HSB-GCS density increases by $\sim$ 3 per cent at each pericentre passage (Martinez-Medina et al. 2022, see their fig. 9), a phenomenon which is called star evaporation[8] (Binney & Tremaine 2008). Lying on the top-right of Fig. 5, they are experiencing much more pericentre passages than other stellar systems. In Fig. 5 their median location is very close to expectations for $f = 0.03$ (see the blue dot-dashed line), which means that they are stellar systems in pseudo-equilibrium with the MW potential and tides. This explains why only few of them possess tails. Because they orbit at low radii, many different processes could generate these tails, such as gravitational interactions with other substructures, for example giant molecular clouds, spiral arms, and the bar (Ibata et al. 2021, and references therein).

This contrasts with LSB-GCs that appear more fragile due to their much lower densities (300 times on average, see Fig. 5), while at significantly larger pericentres, that is, their orbits may extend to regions far from the MW disc. 24 per cent of them are fully tidally shocked, and they are more affected by tides than HSB-GCs, since their locations in Fig. 5 are generally well below the $f = 0.03$ line. Conversely to HSB-GCs, their passages to pericentre are relatively rare, and then their properties are not fully shaped by the MW potential, yet.

HSB-GCs are in pseudo-equilibrium with the MW potential. Going further to the bottom-left of Fig. 5, one finds LSB-GCs that are much less at equilibrium. In the next section we examine whether or not dwarfs galaxies that lie at the very bottom-left of Fig. 5 are in equilibrium.

We have verified that all the above properties, including the relative locations of both GCs and dwarf galaxies relatively to the equality line in Fig. 5, do not change with the MW potential.

## 4 DWARF GALAXY PROPERTIES

### 4.1 Comparison of dwarf galaxy and LSB-GC properties

Fig. 5 shows that LSB-GCs have more similarities in the investigated properties with dwarf galaxies (full triangles) than with HSB-GCs. First, both populations show a fraction of fully tidally disrupted systems, that is, those below the equality line in Fig. 5. The three dwarf galaxies below the equality line are Sgr, Crater II, and Antlia II. The first is well known for its gigantic system of tidal streams that surround the MW (Ibata et al. 2001), and the other two, by their extremely low stellar density and large sizes. Antlia II is likely associated with tidal tails, which is also suspected for Crater II[9] (Ji et al. 2021). Secondly, two LSB-GCs (Pal 3 and Crater) lie in the sequence delineated by dwarfs in Fig. 5. This corroborates Marchi-Lasch et al. (2019) conclusions that structural properties of UFDs and of low surface brightness GCs could be rather similar.

However, none of the 24 remaining dwarfs that lie above the equality line show tidal tails[10] (Hammer et al. 2020), while some LSB-GCs do. In addition, most dwarf galaxies do not show a spherical morphology, and their surface brightness are generally fainter than that of LSB-GCs.

### 4.2 A strong anticorrelation between structural and orbital dwarf properties

In Fig. 5, 24 of the 26 dwarf galaxies appear at first glance to be unaffected by MW tidal shocks due to their location well above the equality line and the absence of tidal tails. However, one may wonder why they delineate a sequence that is precisely parallel and offset by $\sim$ + 1.5 dex to the equality line, with a significance of $\rho = 0.66$ ($P = 8.6 \times 10^{-4}$). The same applies after examining the two panels of Fig. 3 where dwarf densities correlates with $R_{\rm peri}$ as well as GCs, though being offset from them. To understand this, we propose to examine the core sample of 24 dwarf galaxies obtained after removing Antlia II and Crater II. In the following, we investigate which combination of their intrinsic properties (e.g. $r_{\rm half}$, $\sigma_{\rm los}$, and $L_V$) correlates the best with orbital properties (e.g. their pericentre, $R_{\rm peri}$) per cent. Since the orbital energy and angular momentum are well related to the pericentre, we consider first correlation with the latter.

Since tidal forces scale with distance to the system centre, and that DM is more extended than stars, one expects that DM can be used to measure the strength of the tides within dwarf galaxies. We propose

[8]Stellar systems passing near their pericentres are likely affected by MW tidal shocks, which increase the internal energy of their stars, resulting in the least bound to be expelled. Then, after GCs have lost mass, they contract adiabatically when leaving the pericentre towards the apocentre.

[9]Both Antlia II and Crater II have been reproduced by a model in which low density systems have lost their gas and are completely out of equilibrium because they are dominated by tides (see Wang et al. 2023, hereafter Paper III).

[10]Carina has been suggested to be with tides (Battaglia et al. 2012), although contamination by LMC debris may discard it (McMonigal et al. 2014), and the 24 dwarf sample does not include Tucana III, which is a unique system by its extremely low pericentre (few kpc) and that possess a tail. Unfortunately there is no robust measurement of Tucana III kinematics.

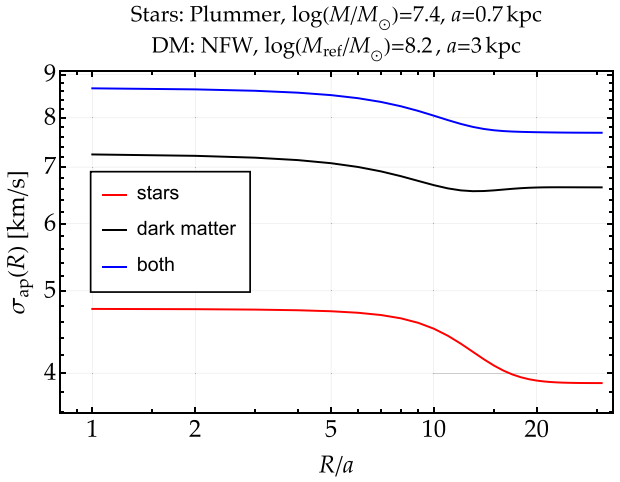


**Figure 6.** Contribution of stars and DM to the velocity dispersion measured in a cylindrical aperture, that is, the average loss velocity dispersion, for a dwarf such as Fornax. Here, $M_{\rm ref} = M_{\rm DM}(a_{\rm dark})$, and isotropic velocities are assumed.

to use the DM contribution to the stellar velocity dispersion as the test for tidal theory, and vice-versa. Its squared value is

$$\sigma^2_{\rm DM} \approx \sigma^2_{\rm los} - \sigma^2_{\rm stars}\ , \tag{10}$$

where $\sigma_{\rm stars}$ is the contribution of stars to the stellar velocity dispersion (the formula is an approximation because of the neglect of the gas component, which appears justified for MW dwarf galaxies). We measure the contribution of the stars to the velocity dispersion, $\sigma_{\rm stars} \equiv \sigma_{\rm ap}(R)$, in a cylindrical aperture of radius $R$ by integrating over the cylinder the stellar contribution to the radial velocity dispersion of the stars, itself found by integrating the Jeans equation of local dynamical equilibrium assuming further isotropic kinematics. This quantity involves a triple integral (one for solving the Jeans equation for the radial component of the 3D velocity dispersion, one for integrating along the line of sight, and one for integrating over the different lines of sight within the aperture). We use the single integral exact expression of equation (B7) of Mamon & Łokas (2005), corrected in Mamon & Łokas (2006), valid for systems with isotropic velocities

$$\sigma^2_{\rm stars} \equiv \sigma^2_{\rm ap}(R) = \frac{4\pi\, G}{3\Sigma(R)} \left[ \int_0^\infty r\nu(r) M(r)\, {\rm d}r - \int_R^\infty \frac{\left(r^2 - R^2\right)^{3/2}}{r^2} \nu(r)\, M(r)\, {\rm d}r \right]\ , \tag{11}$$

where $\nu(r)$ and $\Sigma(R)$ are the 3D and surface stellar number density profiles, respectively, while $M(r)$ is the total mass profile[11]. Fig. 6 gives an example for Fornax, assumed to be embedded in a DM halo.

The top panel of Fig. 7 shows that when removing quadratically $\sigma_{\rm stars}$ the correlation reaches a slightly higher significance, that is, $\rho = 0.74$ between $(\sigma^2_{\rm los} - \sigma^2_{\rm stars})/r_{\rm half}$ and $R_{\rm peri}$, which is associated to a low probability that it occurs by chance, $P = 4.8 \times 10^{-5}$.

Fig. 8 shows how slope, correlation significance, and probability are changing with X when considering the relation in logarithmic scale between $(\sigma^2_{\rm los} - \sigma^2_{\rm stars})\, r^X_{\rm half}$ and $R_{\rm peri}$ for 24 dwarf galaxies. It shows that the correlation peaked at $X = -1$, which likely drives all correlations at $X < -1$.

Anticorrelations shown in Figs 3, 7, and 8 between by dwarf galaxy structural and orbital parameters have already been identified

[11]The original triple integral ensures that equation (11) is a very good approximation to the aperture velocity dispersion for systems with anisotropic velocities.

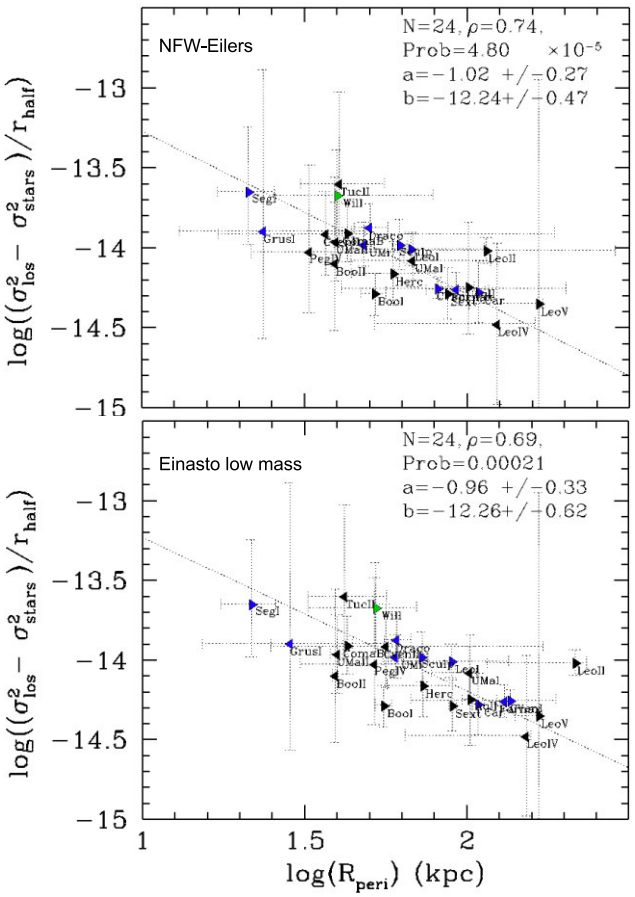


**Figure 7.** Free-fall tidal shocks (or DM) acceleration (in km s$^{-2}$) based on dSph kinematics ($(\sigma^2_{\rm los} - \sigma^2_{\rm stars})\, r^{-1}_{\rm half}$) versus pericentre radius. Data ($\sigma_{\rm los}$, $L_V$, $r_{\rm half}$) come from table B1 of Appendix B.

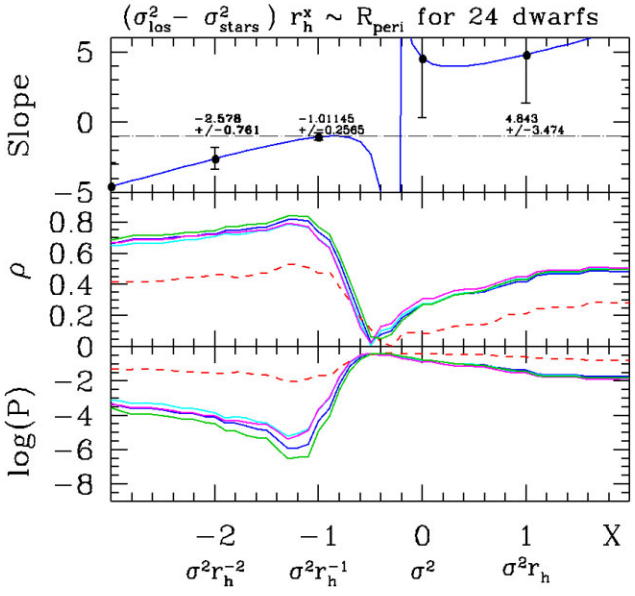


**Figure 8.** Slope, correlation $\rho$ (its absolute value), and associated probability (in logarithmic scale) of the correlation between $(\sigma^2_{\rm los} - \sigma^2_{\rm stars})\, r^X_{\rm half}$ and $R_{\rm peri}$ (red-dashed line: with $R_{\rm GC}$) from $X = -3$ to $X = 2$. Each quantity is shown on the $X$ axis and $\rho$, and associated probability are given for the 4 MW mass models (see coloured lines).

by Hammer et al. (2019), who also considered $\sigma^2_{\rm los} - \sigma^2_{\rm stars}$, and by Kaplinghat, Valli & Yu (2019), who found robust anticorrelations between 3D density within 150 pc and pericentre (see their fig. 2). However, Kaplinghat et al. (2019) found that the anticorrelation vanishes for UFDs. This difference can be explained because, in contrast to us, they include both Antlia II and Crater II in the UFD sample, and both objects dominate the relation because of their extremely low densities (see their fig. 3). We re-assess that Antlia II and Crater II (as well as Sgr) are experiencing strong tidal stripping conversely to the rest of the 24 dwarfs considered here, as it is shown in Fig. 5. We confirm the Kaplinghat, Valli & YuKaplinghat et al. result, that is, by inserting Antlia II and Crater II in Figs 3, 7, and 8 is sufficient to wash out the anticorrelation, because they have densities several dex lower than those of other dwarfs.

If MW dwarf galaxies were at self-equilibrium with their own gravity, both $(\sigma^2_{\rm los} - \sigma^2_{\rm stars})/r_{\rm half}$ and $(\sigma^2_{\rm los} - \sigma^2_{\rm stars})/r^2_{\rm half}$ would correspond to the surface and 3D mass densities of the sole DM component.[12] Looking at the slope of the correlations (see top panel of Fig. 8), it implies that both quantities vary as $R^{-1}_{\rm peri}$ and $R^{-2.6}_{\rm peri}$, respectively. If dwarf galaxies were long-term satellites of the MW, this could be interpreted as being caused by a 'survivor bias', that is, satellites with small pericentre would be those having been shielded against the tidal forces (see Vitral & Boldrini 2022), which means that they have to be denser (Kaplinghat et al. 2019), even favouring cusped density profiles in their centre (Errani et al. 2023). Assuming that MW dwarfs are long-term satellites, Robles & Bullock (2021) found that subhalos with small pericentres are indeed denser after a Hubble time evolution, while Kravtsov & Wu (2023) did not.

However, due to their high orbital energy and angular momenta, most dwarf galaxies are stellar systems that arrived late in the MW halo (less than 3 Gyr ago, see Paper I). It results that they have no time to make one or few orbits in the MW halo, in sharp contrast with a long-term satellite hypothesis. It thus appears quite enigmatic why their structural parameters such as $r_{\rm half}$ and $\sigma_{\rm los}$ show a correlation with orbital parameters in Fig. 7 and with the tidal-shock characteristic time in Fig. 5.

## 5 DISCUSSION

### 5.1 Dwarf galaxies with escaping stars affected by MW tides

Fig. 8 also shows that the correlations with pericentre ($R_{\rm peri}$) are much stronger than with galactocentric radius ($R_{\rm GC}$, red line). This suggests that intrinsic properties of dwarf galaxies are linked to MW tides (see also Section 5.3 for a more detailed discussion). This calls for a mechanism related to the expected progenitor properties of MW dwarfs, a few Gyr ago. Section 5.7 discusses the impact of a dwarf recent infall onto their DM properties.

Beyond 300 kpc, all dwarfs (but a few, e.g. Cetus and Tucana) are gas-rich, while they are gas-poor within 300 kpc (except the massive LMC/SMC; Grcevich & Putman 2009). If the former are progenitors of the latter, gas-rich dwarfs are expected to be stripped during their infall due to the ram pressure caused by the Galactic halo gas (Mayer et al. 2006). The role of the removed gas during the process could be essential, if it induces a lack of gravity implying that many stars have to expand (Grishin et al. 2021) following a spherical geometry (for an isotropic distribution of initial velocities of stars). The fraction of stars that are lost depends on the total initial mass, on the mass

[12]This is roughly true for isotropic, isothermal systems.

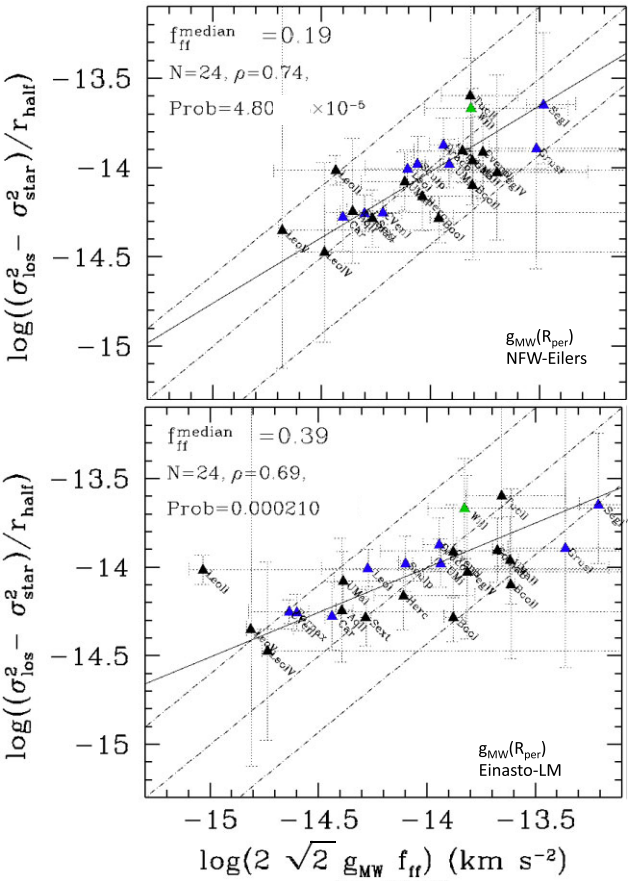


**Figure 9.** Free-fall tidal shocks (or DM) acceleration (in km s$^{-2}$) based on dSph kinematics ($(\sigma^2_{\rm los} - \sigma^2_{\rm stars})/r_{\rm half}$) versus MW gravity at pericentre, for the NFW (*top panel*) and Einasto low mass (*bottom panel*) MW models. The *solid line* represents the best fit of the correlation, whose characteristic numbers are provided in the top-left. The line corresponding to the median of $f_{\rm ff}$ is the central dot-dashed line, while the two other *dot-dashed lines* correspond to the median value, multiplied (*top line*) or divided (*bottom line*) by 2.5, respectively.

fraction initially represented by the gas, and also on the relative size of the different components in the progenitor.

Simulations performed by Yang et al. (2014) have shown that when the gas is lost near the pericentre passage, it increases the dwarf kinematics, because many stars are escaping the system and are then affected by the MW gravity. Hammer et al. (2020) proposed an ideal case for which a fraction ($f_{\rm ff}$, ff standing for free-fall) of stars are not affected by the dwarf self-gravity, but by the MW gravity. Assuming a Plummer profile for the dwarf, they calculated that the dwarf squared velocity dispersion is increased by

$$\Delta\sigma^2 = 2\sqrt{2}\, g_{\rm MW}\, r_{\rm half}\, f_{\rm ff}, \qquad (12)$$

where $g_{\rm MW}$ stands for the MW gravity.[13] equation (12) is oversimplified since in reality, stars lying in the centre may move sufficiently fast that they are adiabatically invariant to the actions of the moving

[13]This comes from an integration of the velocity dispersion along the line of sight for stars assumed to be free falling into the MW gravitational field. However this is quite a simplification since the stars, even the unbound ones that have just escaped the cluster or dwarf, move in the combined gravity of its parent system and the MW. The first term $2\sqrt{2}$ would be changed into $2.08\sqrt{2}$ for a perfect sphere model (Hammer et al. 2018b).

MW gravitational field (Weinberg 1994; Binney & Tremaine 2008). Some of our simulations (Paper III) show a residual core that appears stable against star expansion and MW gravity. This is an adiabatic effect, since the most bound stars have very short orbital periods compared to the time-scale of the MW flyby. So, for the encounter, they appear smeared along their internal cluster orbits, and the external perturbation can only kick the orbit as a whole (i.e. mainly linear momentum exchange). For the cluster envelope stars, the flyby is impulsive, they only cover a fraction of its orbits during the flyby, so the external perturbation can do work deforming their orbits (i.e. mainly energy exchange), heating up their dynamics and contributing to their expansion and eventually becoming unbound.

The consequence would be to change $f_{\rm ff}$ in equation (12) into a smaller value if stars within $r_{\rm half}$ are less affected due to adiabatic invariance. Simulations also show that the gas removal is a turbulent process that affects both gas and star motions during the time they are bound together, and also affect the velocity dispersion of stars after gas removal. In the following equation, we consider this to be accounted for by the $f_{\rm ff}$ factor, which depends also on the structural properties of the dwarf. We derive

$$\frac{\sigma^2_{\rm los} - \sigma^2_{\rm stars}}{r_{\rm half}} = 2\sqrt{2}\, g_{\rm MW}\, f_{\rm ff}, \tag{13}$$

Fig. 9 shows that $(\sigma^2_{\rm los} - \sigma^2_{\rm stars})/r_{\rm half}$ correlates well with the MW gravity, with a similar correlation strength than that with pericentre. For the NFW MW mass model (top panel) tidal shocks exerted on expanding stars can reproduce the observations if the fraction ($f_{\rm ff}$) of the latter ranges from 0.08 (bottom dot-dashed line) to 0.48 (top dot-dashed line), with a median at 0.19. Classical dwarfs, but Leo II, are mostly near the median value, as well as most dwarfs of the VPOS (blue triangles, see, e.g. Pawlowski et al. 2012), but Grus I.

When adopting the low MW mass model (bottom panel of Fig. 9), $f_{\rm ff}$ ranges from 0.16 to 0.98, with a median value of 0.39. However, Leo II appears as an outlier ($f_{\rm ff} > 1$), which could be caused by the quite large uncertainty on the MW acceleration at pericentre, or alternatively, because it does not obey equation (13).

Fig. 10 confirms our finding (see Fig. 8) that the correlation with $g_{\rm MW}$ is driven by $X = -1$, which supports the validity of equation (13), and then the fact that intrinsic properties such as $\sigma_{\rm los}$ and $r_{\rm half}$ are changing through a temporal sequence, gas removal, star expansion, and then MW tidal shocks. It also shows that the correlation is much improved when adopting MW gravity at pericentre (see the red-dashed line representing gravity at $R_{\rm GC}$), suggesting further a tidal origin for the observed correlations.

We notice that Fig. 10 is essentially similar than Fig. 8 probably because in the range of pericentre values, $g_{\rm MW}$ values are simply set by $R_{\rm peri}$ values. However, it provides a good test for the validity of equation (13).

### 5.2 Comparison with numerical simulations

A physical interpretation of the correlation shown in Fig. 9 may need two conditions to be fulfilled at the time dwarfs are observed:

(i) due to the gas removal and gravity loss a significant fraction of stars are expanding to the dwarf outskirts and are gradually less affected by the dwarf gravity;

(ii) gas loss happened at a time quite close from that of the pericentre passage, which resulted in many of the stars in the dwarf outskirts to be tidally shocked by the MW.

The first condition is fulfilled if the gas represents ∼50 per cent of the baryonic mass within the initial half-mass radius of the

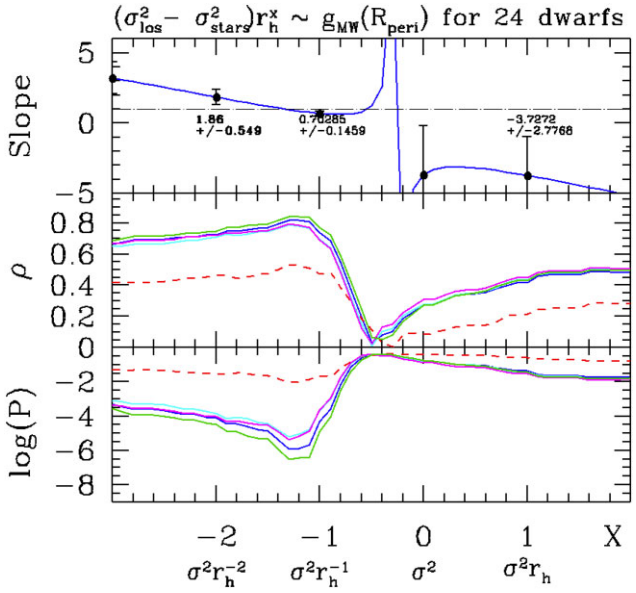


**Figure 10.** Slope, correlation $\rho$, and associated probability (in logarithmic scale) of the correlation between $(\sigma^2_{\rm los} - \sigma^2_{\rm stars})\, r^X_{\rm half}$ and $g_{\rm MW}$ at $R_{\rm peri}$ (red-dashed line: at $R_{\rm GC}$) from $X = -3$ to $X = 2$, respectively. Each quantity is shown on the $X$ axis, and associated probability are given for the 4 MW mass models (see coloured lines).

dwarf progenitor. For example, such a condition is well reached for the dwarf irregular WLM (Yang et al. 2022b) that has a stellar mass similar to that of Fornax (McConnachie 2012). The second condition is likely reached because there is a significant excess of dwarf spheroidal and UFDs lying near pericentre (Fritz et al. 2018; Hammer et al. 2020; Li et al. 2021), where both ram pressure and tidal forces are maximal.

Simulations by Yang et al. (2014) have shown that their initial dwarf 3 is able to reproduce the flat velocity dispersion radial profiles of UMi or Draco. It also reproduces morphologies and surface-brightness of the two dwarfs (see also figs 10 and 11 of Hammer et al. 2018b). In these simulations a significant part of the initial stars has been lost during the dwarf infall in the MW halo, due to their expansion after gas removal.

More simulations are needed to verify whether each MW dwarf can be reproduced in this way, including the more massive ones, for example Sculptor (see Paper III), as well as UFDs. One difficulty is numerical, for example it is essential to ensure a high resolution and thus small mass for the stellar and gas particles in the dwarfs, the latter of which have to interact with MW hot gas particles, the total mass of which is a hundred to a thousand times larger than that of the initial dwarfs. Comparison between simulations and observations needs to consider all stellar particles, including those that are just in projection on the dwarf core since they also contribute to $\sigma_{\rm los}$ (see, e.g. bottom-left panel of Fig. 11).

Simulations of Paper III show that if the above conditions (i), and (ii) are granted, the velocity dispersion (bottom-right panel of Fig. 11) is much higher than expectations from self-equilibrium of the stellar component alone (compare the dashed green line with the solid blue line). This increase is found maximal at pericentre passage (T∼ 4.5 Gyr, see top-left panel of Fig. 11), while such a phenomenon has a duration of several hundred of million years. This is indicated by Fig. 11 that represents the stellar particle properties at T = 5 Gyr (see the red star in the top-left panel), when velocity dispersion is still considerably increased (compare blue solid and green dash lines in

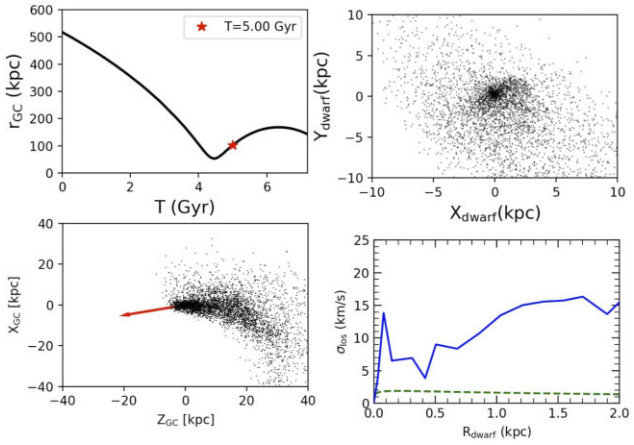


**Figure 11.** Evolution of stars in a hydrodynamical simulation made in Paper III and based on a MW mass model of $8 \times 10^{11}$ $M_{\odot}$, with a halo gas mass density following that has been adopted by Wang et al. (2019) to reproduce the Magellanic stream. In this simulation the DM halo is truncated at $r_{200} = 189$ kpc. *Top-left panel* gives the trajectory of the dwarf (Galactocentric distance versus time) that follows that of Sculptor, whose star properties are captured 0.5 Gyr after pericentre passage (*see the red point in the top-left panel*). *Top-right* panel indicates that a significant fraction of stars have left the main body of the dwarf while *bottom-left panel* shows that it brings an additional extended component mostly along the line of sight (indicated by the *red arrow*). *Bottom-right panel* shows the radial profile of the line-of-sight velocity dispersion similarly to measurements currently made for MW dwarfs (*blue solid line*) and compare it to expectations from equilibrium with its stellar mass content (*green dash line*). More details will be given in Paper III.

bottom-right panel). This additional velocity dispersion is provided by stars unbound to the dwarf, which are affected by tidal shocks as expected from equation (9). The situation in the central core of the dwarf is probably more complex, since ∼300 Myr after the gas release, there are still stars that are in expansion because of their large velocity, while some other core stars can also be affected by tidal shocks since their small velocity may place them in the impulse approximation conditions.

### 5.3 Combination of tidal shocks and ram-pressure stripping

Fig. 11 also illustrates that equation (13) is too simplistic in assuming that all the energy exchange ($\Delta E = \sigma^2/2$) occurs only along the line of sight, especially if the main contribution occurs at pericentre. In reality, the exchange of energy should result from an integration over all the past orbit of the dwarf galaxy. It would affect the validity of equation (13) especially for nearby dwarf galaxies, for which the direction of $g_{MW}$ when calculated at pericentre may differ from the line of sight. This could explain why the correlation slope in Fig. 9 is smaller than 1, that is, because the X-axis value could have been overestimated for nearby dwarfs, such as Segue I or Grus I that lie on the right of the Fig. 9.

Another limitation of equation (13) is that in addition to MW tidal shocks, gas removal also leads to an increase of the dwarf velocity dispersions. This is because after gas loss, stars keep the memory of their initial velocity dispersion, which is large because it balanced the initial total mass of both gas and stellar components. Since ram pressure stripping is also expected to be maximal near pericentre, it could contribute to the correlations found in Figs 7 and 9, in addition to tidal shocks described by equation (13).

Paper III shows that this could explain the larger velocity dispersion of Antlia II when compared to that of Crater II. The latter, having not passed its pericentre, is mostly affected by the gas removal, while the former, having passed its pericentre, is furthermore affected by tidal shocks. Reproducing the excess of velocity dispersion in all dwarfs, including UFDs, would require a specific modelling of each of them. Besides numerical limitations discussed earlier, this is also complicated by the fact that new observations from deeper surveys (e.g. from Cantu et al. 2021 and Chiti et al. 2022) have shown that structural parameters such as the half-light radius of Grus I may have changed from 28 to 151 pc. On the other hand, UFD orbits often have larger eccentricity than classical dwarfs, which suggests a better efficiency of MW tidal shocks.

### 5.4 Consistency of dwarf infall times with their star formation histories

A scenario for which MW halo gas and gravity has recently shaped the dwarf morphologies and kinematics differs with results of many previous studies, for which constraints about infall times of MW dwarf galaxies were mostly coming from their star formation histories.

While some classical dwarfs have extended star-formation histories (Fornax, Carina, LeoI, Leo II, Canes Venaciti I), some other (Sculptor, Sextans, Ursa Minor, and Draco) show only very old stellar populations (see, e.g. Weisz et al. 2014). Many UFDs share the latter property, though the result is less robust given the lack of RGB stars to determine age and metal abundances (Vanessa Hill, 2019, private communication). This has led some studies to assume very early infall events for most dwarfs, even reaching the ionization epochs (Seo & Ann 2023, and references therein). It has also been attempted to reconcile infall times with star formation histories (Rocha et al. 2012; Fillingham et al. 2019; Miyoshi & Chiba 2020; Barmentloo & Cautun 2023), on the basis that the dwarf gas is likely to be stripped during the infall, or alternatively, could be removed by other mechanisms (e.g. feedback from supernovae and mergers) at very early epochs.

However, star formation histories may not unequivocally trace the orbital history. As a first counter example, Draco, Ursa Minor, Carina, and Canes Venaciti I share similar stellar mass and orbital energy within 0.2 dex (factor 1.6), which suggests similar infall times. However, the former two show no star formation since almost 10 Gyr, and the two latter have a star formation still active 1.5–2 Gyr ago (Martin et al. 2008; Weisz et al. 2014). A second example is provided by UFDs that may have not been able to form stars before their infall to the MW halo because of their too small gas surface density, which is likely below the Schmidt–Kennicutt law (Kennicutt 1998).

Predicting the orbital history from the star formation history requires accounting for the very last star formation event, even if it corresponds to a very small fraction of the stellar mass. Fornax provides a good illustration of this, because de Boer et al. (2013) found a new stellar over-density, located 0.7 kpc from the centre, which is only 100 Myr old, but accounts for a tiny fraction of the stars. This indicates that the last part of its gas has left Fornax very recently.[14], likely through ram-pressure exerted by the MW halo hot gas. A recent gas removal is consistent with a recent first infall for which the ram-pressure may have slowed it down reducing its orbit eccentricities (see Paper III). Conversely, a first infall 8 Gyr

[14]Part of this gas may have been directly detected as a very large H I gas cloud superposed on Fornax (Bouchard, Carignan & Staveley-Smith 2006).

ago is unlikely, because Fornax would have accomplished about 4 pericentre passages since then which should have removed the gas much earlier than 100 Myr ago[15]

Having many dwarfs entering the MW halo 8–10 Gyr ago is in sharp contradiction with the orbital energy-infall time correlation shown in fig. 1 of Rocha et al. (2012; see also fig. 6 of Paper I, as well as Appendix A and Fig. A1). This is because such an epoch coincides with that of the GSE event, which shows an orbital energy 5 (0.7 dex) times smaller than the average energy of dwarfs (see Appendix A).

A recent infall of most MW dwarf galaxies predicts:

(i) less than 3 Gyr ago they were gas-rich and they have lost their gas near their first pericentre passage;
(ii) before being removed, the gas is pressurized by the MW hot corona, which leads to star formation, and at least a small fraction of young stars is expected to be found in their cores;
(iii) the fraction of young stars depends on whether young stars are kept in the central core or are expanding in the dwarf outskirts.

For Fornax, de Boer et al. (2012) measured that only a few per cent of stars are younger than 2 Gyr. The most interesting dwarfs to test are Sculptor, Ursa Minor, and Draco, for which colour–magnitude diagrams (CMDs) are sufficiently populated (de Boer et al. 2011; Muñoz et al. 2018), and that are fully dominated by old stars (de Boer et al. 2012; Weisz et al. 2014). Yang et al. (2023, in preparation, hereafter Paper IV) has re-analysed CMDs of these classical dwarfs among others. They found evidence for massive and young stars that lie on the blue side of the RGB branch. In particular, Sculptor, Ursa Minor, and Draco contain a small fraction of young stars, implying recent gas loss, consistent with a recent infall less than 3 Gyr ago. Simulations of Paper III predict that young stars formed during a ram-pressure event have their motions strongly affected by the gas that is leaving the dwarf. Consequently, these simulations of Paper III suggest that only a small fraction of young stars stay in the core, in agreement with observations (see Paper IV).

### 5.5 Predictions of stellar halos surrounding dwarf galaxies

The scenario of a recent accretion of gas-rich MW dwarfs, accompanied by a recent gas removal, followed by stellar expansion, and efficient MW tidal shocks, predicts that dwarf outskirts should be populated well beyond their half-light radii. Simulations of such a combination of effects show (see Fig. 11) that a significant part[16] of the initial stellar content of the dwarf galaxy is expelled into the MW halo (see Section 5.1). Fig. 11 predicts that most dwarfs affected by this effect should be accompanied by expanding stars in their outskirts, while the distance they have covered depends on the epoch when the gas has been removed and if the outer DM could have been tidally stripped after a single passage.

While investigations of dwarf outskirts is a very novel field mostly based on *Gaia* observations, recent studies have found member stars lying far or very far from dwarf galaxy cores. Fornax has been intensively studied by Yang et al. (2022a), and they found an additional component in its outskirts. More recently, the combination of *Gaia* and high resolution spectroscopy has convincingly detected the presence of stars from 4 to 12 $r_{\rm half}$ in Ursa Minor (Sestito et al. 2023), Ursa Major I, Coma Berenices, Bootes I (Waller et al. 2023), Tucana II (Chiti et al. 2023), and Sextans (Roederer et al. 2023). In addition, when observing Grus I by using a much deeper photometry than Muñoz et al. (2018), Cantu et al. (2021) found a considerably much larger size, with a half-light radius increased by a factor over five: passing from 28 pc to 151 pc.

Future observations will show whether there are evaporating stars in most MW dwarfs, which is expected if they are expanding stellar systems after gas and gravity losses.

### 5.6 Could the correlations be generated by selection effects?

The strong correlations found in Figs 7 and 9 are likely responsible for most correlations shown by dwarf galaxies all along this paper. Their impact is strong because they correspond to a theoretical prediction (see equation (13)), for which MW dwarf galaxies are stellar systems out of equilibrium due to the severe impact caused by the gas removal and MW tidal shocks. However, one may wonder if there could be selection effects, for example due to the fact that not all the MW dwarfs have been discovered, or for which their velocity dispersion has not been determined, yet.

The top panel of Fig. 12 reveals the trend between dwarf visible luminosity and galactocentric distance. This could be due to selection effects as faint dwarfs are more difficult to be detected at larger distances (Drlica-Wagner et al. 2020).

This may generate the anticorrelation between $M_{\rm tot}/L_{\rm V}$ and $R_{\rm GC}$, because $M_{\rm tot}$ has been calculated from equation (3), and does not correlate with $R_{\rm GC}$ (see red-dashed lines in Fig. 8 for $X = 1$).

One may wonder whether or not this possible selection effect can also be responsible of the correlations found in this paper. Fig. 13 provides a negative answer, because the structural parameter that is the most correlated with the pericentre, $(\sigma^2_{\rm los} - \sigma^2_{\rm stars})/r_{\rm half}$, is not correlated with $L_V$. It results that the correlations between $(\sigma^2_{\rm los} - \sigma^2_{\rm stars})/r_{\rm half}$ and $R_{\rm peri}$ or $g_{\rm MW}$ are unlikely to be affected by selection effects.

### 5.7 Are MW dwarf DM contents over-estimated?

A recent arrival of most dwarfs in the MW halo, together with recent bursts of star formation, favours a scenario in which they have recently lost their gas, making them unstable against MW tides. The fact that most dwarfs are near their pericentre also supports the recent loss of gas together with MW tidal shocks. This is indicated by the correlations shown in Figs 7 and 9, which are theoretically predicted, as well as reproduced by simulations of Paper III.

However, we notice that the recent infall of MW dwarfs is justified by orbital arguments, with a timing scale coming from comparisons to former merger events in the MW halo (e.g. GSE and Sgr). This would have considerable consequences on the DM content of dwarf progenitors and then on that of MW dwarfs. As shown by Mayer et al. (2006), it would require several pericentre passages and a Hubble time to transform a DM-dominated rotating gas-rich dwarf into a gas-free, dispersion supported system. Here, this transformation needs to be done in just one orbit, which considerably limits the possible amount of DM. Paper III has simulated a DM-dominated progenitor of Sculptor, assuming the prescription from equation (3), which has been established by Wolf et al. (2010). It confirms that in the Sculptor

[15]This is because the gas of the MW has been already tested at large distance from the modelling of the Magellanic Stream, from which it should reach density of $10^{-4}$ atoms cm$^{-3}$ at 100–200 kpc (Hammer et al. 2015; Wang et al. 2019), values sufficiently high to strip Fornax gas in less than 2 orbits.
[16]Even without recent gas stripping and tidal shocks, there is always a floor non-zero value of stars evaporating in a self-gravitating system. In the future on may compare predictions of Fig. 11 with simulations of systems lacking gas (no gas removal effect) and in circular orbits of radius equal to the present galactocentric distances (no tidal shocks).

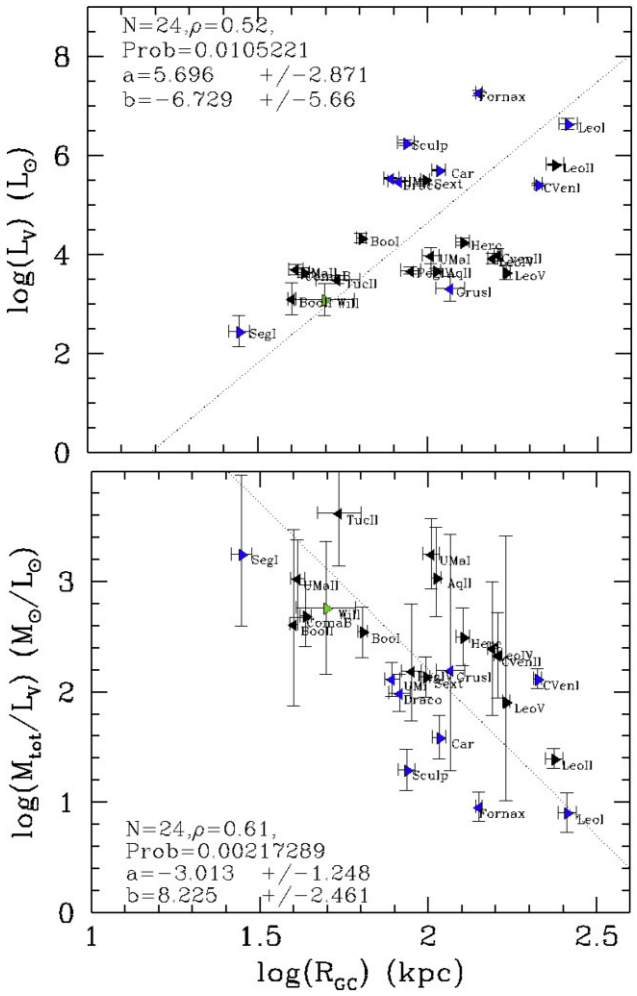


**Figure 12.** Correlation between $V$-band luminosity $L_V$ (*top panel*) and $M_{\rm tot}/L_V$ (*bottom panel*) with the galactocentric radius $R_{\rm GC}$.

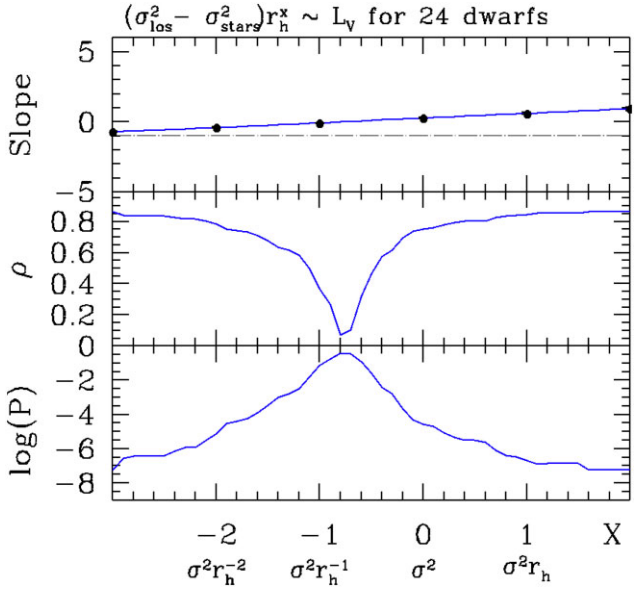


**Figure 13.** Slope, correlation $\rho$, and associated probability (in logarithmic scale) of the correlation between $\sigma^2_{\rm los} r^X_{\rm half}$ and $L_V$ from $X = -3$ to $X = 2$. Each quantity is shown on the $X$ axis.

orbital conditions, a rotating gas-rich dwarf cannot be transformed into a MW gas-free dwarf after one orbital time.

This scenario implies that most MW dwarfs as they are observed today are not in equilibrium. Their recent gas removal together with MW tidal shocks suffice to explain their high velocity dispersions, both from theory and simulations. It results that the self-equilibrium conditions assumed by Walker et al. (2009) and Wolf et al. (2010) cannot apply to MW dwarf galaxies, which questions the corresponding estimates of large mass excess when they are compared to the stellar mass. Consequently, this means that we have no way to prove or disprove the presence of DM in objects far from equilibrium.

## 6 CONCLUSIONS

Here, we have investigated how the structural (morphological and kinematical) properties of MW GCs and dwarf spheroidals depend on their orbital properties. We have further limited our investigations to relations that do not depend on the adopted MW mass. We first confirm that the $r_{\rm half} \propto 1/E$ relation found in Paper I is robust to the adopted MW mass model.

We also confirm that HSB-GCs are in pseudo-equilibrium with MW tidal shocks, removing approximately 3 per cent of their mass at each pericentre passage. They differ from the more fragile LSB-GCs, which are strongly destabilized by MW tides, a significant fraction of them (27 per cent) possess tidal tails, and/or are in a tidal dominant regime (24 per cent, see Fig. 5).

Dwarf galaxies show some similarities with LSB-GCs. However, correlations between their structural and orbital properties are unexpected if they arrived recently into the MW halo and have no time to perform more than one orbit (see Paper I). Specifically the anticorrelation shown in Fig. 7 or that found by Kaplinghat et al. (2019, see their fig. 1) is in tension with MW dwarfs modelled as systems at self-equilibrium with large amounts of DM. Indeed, it is difficult to explain why new-coming sub-halos have their densities depending on pericentre without having time to be affected by MW tides (Cardona-Barrero et al. 2023).

A late infall for dwarfs requires one to consider the properties of their pre-infall progenitors outside the MW halo. They are likely gas-rich dwarf galaxies (Grcevich & Putman 2009), and their passage into the MW halo gas may have fully transformed them into gas-free dwarf galaxies (Mayer et al. 2006; Yang et al. 2014). It suggests that most dwarf properties result from a temporal sequence, beginning with gas stripping due to MW halo gas ram-pressure, expansion of their stars due to the subsequent lack of gravity, and then a significant impact of MW tidal shocks exerted mostly on the leaving stars. The impact of such an out-of-equilibrium process has been theoretically described, and will be shown in Paper III simulations, for which a first example is provided in Fig. 11. It is also consistent with the dwarf proximity to their pericentres, a property that otherwise would appear in contradiction with conservation of energy.

This scenario allows us to make the following predictions: most MW dwarf galaxies (1) have velocity dispersion values with a significant contribution due to ram-pressure stripping and Galactic tidal shocks; (2) show many stars in their outskirts, their distances from the dwarf core depending on the elapsed time since the gas has been decoupled from stars; and (3) show a small fraction of young stars, both in their cores and outskirts.

Condition (1) is fulfilled through equation (13) and Fig. 9, as well as from simulations. Verification of condition (2) is on-going through the recent and successful discoveries of stars in the very outskirts of dwarfs (Cantu et al. 2021; Yang et al. 2022a; Chiti et al. 2023; Roederer et al. 2023; Sestito et al. 2023; Waller et al. 2023). Paper

IV reveals that condition (3) is also fulfilled on the basis of a novel investigation of their CMDs. This series of papers (Papers I–IV) may change our understanding of MW dwarf galaxies, passing from an equilibrium model allowing mass estimates, to an out-of-equilibrium model that prevents mass estimates other than that of the baryonic mass.

Further simulations could be useful to verify which amount of DM they may contain for allowing their transformation into gas-free, dispersion-supported dwarfs in a single orbit, while preserving the correlations shown in Figs 7 and 9.

## ACKNOWLEDGEMENTS

We warmly thank the referee, Dr Luis Alberto Aguilar, for his very useful report, from which we confess having adopted some sentences in the final version, because they better convey the physics underlying this paper. We are grateful for the support of the International Research Programme Tianguan, which is an agreement between the CNRS in France, NAOC, IHEP, and the Yunnan University in China. J-LW acknowledges financial support from the China Scholarship Council (CSC) No. 202210740004, as well as Y-JJ (No. 202108070090). MSP acknowledges funding of a Leibniz-Junior Research Group (project number J94/2020).

## DATA AVAILABILITY

All necessary data used in this paper are available in the tables of the Appendix B and in Li et al. (2021).

## REFERENCES

Aguilar L. A., White S. D. M., 1985, ApJ, 295, L374
Aguilar L., Hut P., Ostriker J. P., 1988, ApJ, 335, L720
Barmentloo S., Cautun M., 2023, MNRAS, 520, 1704
Battaglia G., Irwin M., Tolstoy E., de Boer T., Mateo M., 2012, ApJ, 761, L31
Baumgardt H., 2017, MNRAS, 464, 2174
Baumgardt H., Hilker M., 2018, MNRAS, 478, 1520
Baumgardt H., Sollima A., Hilker M., 2020, PASA, 37, e046
Baumgardt H., Vasiliev E., 2021, MNRAS, 505, 5957
Binney J., Tremaine S., 2008, Galactic Dynamics: Second Edition. Princeton University Press, New Jersey
Bouchard A., Carignan C., Staveley-Smith L., 2006, AJ, 131, 2913
Bovy J., 2015, ApJS, 216, 29
Boylan-Kolchin M., Bullock J. S., Sohn S. T., Besla G., van der Marel R. P., 2013, ApJ, 768, L140
Bruce J., Li T. S., Pace A. B., Heiger M., Song Y.-Y., Simon J. D., 2023, ApJ, 950, L167
Caldwell N., et al., 2017, ApJ, 839, L20
Cantu S. A., et al., 2021, ApJ, 916, L81
Cardona-Barrero S., Battaglia G., Nipoti C., Di Cintio A., 2023, MNRAS, 522, 3058
Cerny W., et al., 2023, ApJ, 942, L111
Chiti A., et al., 2023, AJ, 165, 55
Chiti A., Simon J. D., Frebel A., Pace A. B., Ji A. P., Li T. S., 2022, ApJ, 939, L41
de Boer T. J. L., et al., 2011, A&A, 528, 119
de Boer T. J. L., et al., 2012, A&A, 544, 73
de Boer T. J. L., Tolstoy E., Saha A., Olszewski E. W., 2013, A&A, 551, 103
Drlica-Wagner A., et al., 2020, ApJ, 893, L47
Eilers A.-C., Hogg D. W., Rix H.-W., Ness M. K., 2019, ApJ, 871, L120
Einasto J., 1965, Trudy Astrofizicheskogo Instituta Alma-Ata, 5, 87
Erkal D., Belokurov V. A., 2020, MNRAS, 495, 2554
Errani R., Navarro J. F., Peñarrubia J., Famaey B., Ibata R., 2023, MNRAS, 519, 384
Fillingham S. P., et al., 2019, preprint (arXiv:1906.04180)
Fritz T. K., Battaglia G., Pawlowski M. S., Kallivayalil N., van der Marel R., Sohn S. T., Brook C., Besla G., 2018, A&A, 619, 103
Garrison-Kimmel S., Boylan-Kolchin M., Bullock J. S., Lee K., 2014, MNRAS, 438, 2578
Gnedin O. Y., Ostriker J. P., 1997, ApJ, 474, L223
Gnedin O. Y., Ostriker J. P., 1999, ApJ, 513, L626
Gott J. Richard, I., 1975, ApJ, 201, L296
Grcevich J., Putman M. E., 2009, ApJ, 696, L385
Grishin K. A., Chilingarian I. V., Afanasiev A. V., Fabricant D., Katkov I. Y., Moran S., Yagi M., 2021, Nature Astron., 5, 1308
Hammer F., et al., 2023, MNRAS, 519, 5059
Hammer F., Flores H., Puech M., Yang Y. B., Athanassoula E., Rodrigues M., Delgado R., 2009, A&A, 507, 1313
Hammer F., Yang Y. B., Flores H., Puech M., Fouquet S., 2015, ApJ, 813, L110
Hammer F., Yang Y. B., Wang J. L., Ibata R., Flores H., Puech M., 2018a, MNRAS, 475, 2754
Hammer F., Yang Y., Arenou F., Babusiaux C., Wang J., Puech M., Flores H., 2018b, ApJ, 860, L76
Hammer F., Yang Y., Arenou F., Wang J., Li H., Bonifacio P., Babusiaux C., 2020, ApJ, 892, L3
Hammer F., Yang Y., Wang J., Arenou F., Puech M., Flores H., Babusiaux C., 2019, ApJ, 883, L171
Haywood M., Lehnert M. D., Di Matteo P., Snaith O., Schultheis M., Katz D., Gómez A., 2016, A&A, 589, 66
Hopkins P. F., et al., 2010, ApJ, 715, L202
Ibata R., et al., 2021, ApJ, 914, L123
Ibata R., Irwin M., Lewis G., Ferguson A. M. N., Tanvir N., 2001, Nature, 412, 49
Jenkins S. A., Li T. S., Pace A. B., Ji A. P., Koposov S. E., Mutlu-Pakdil B., 2021, ApJ, 920, L92
Ji A. P., et al., 2021, ApJ, 921, L32
Jiao Y., Hammer F., Wang J. L., Yang Y. B., 2021, A&A, 654, 25
Kaplinghat M., Valli M., Yu H.-B., 2019, MNRAS, 490, 231
Kennicutt Robert C. J., 1998, ApJ, 498, L541
King I. R., 1966, AJ, 71, 64
Kravtsov A., Wu Z., 2023, MNRAS, 525, 325
Kruijssen J. M. D., et al., 2020, MNRAS, 498, 2472
Kruijssen J. M. D., Pfeffer J. L., Reina-Campos M., Crain R. A., Bastian N., 2019, MNRAS, 486, 3180
Li H., Hammer F., Babusiaux C., Pawlowski M. S., Yang Y., Arenou F., Du C., Wang J., 2021, ApJ, 916, L8
Malhan K., et al., 2022, ApJ, 926, L107
Mamon G. A., Łokas E. L., 2005, MNRAS, 362, 95
Mamon G. A., Łokas E. L., 2006, MNRAS, 370, 1581
Marchi-Lasch S., et al., 2019, ApJ, 874, L29
Martin N. F., et al., 2008, ApJ, 672, L13
Martinez-Medina L. A., Gieles M., Gnedin O. Y., Li H., 2022, MNRAS, 516, 1237
Mayer L., Mastropietro C., Wadsley J., Stadel J., Moore B., 2006, MNRAS, 369, 1021
McConnachie A. W., 2012, AJ, 144, 4
McMillan P. J., 2017, MNRAS, 465, 76
McMonigal B., et al., 2014, MNRAS, 444, 3139
Miyoshi T., Chiba M., 2020, ApJ, 905, L109
Muñoz R. R., Côté P., Santana F. A., Geha M., Simon J. D., Oyarzún G. A., Stetson P. B., Djorgovski S. G., 2018, ApJ, 860, L66
Naidu R. P., et al., 2021, ApJ, 923, L92
Navarro J. F., Frenk C. S., White S. D. M., 1996, ApJ, 462, L563
Ou X., Eilers A.-C., Necib L., Frebel A., 2023, preprint (arXiv:2303.12838)
Pagnini G., Di Matteo P., Khoperskov S., Mastrobuono-Battisti A., Haywood M., Renaud F., Combes F., 2022, A&A, 673, 86
Patel E., et al., 2020, ApJ, 893, L121
Pawlowski M. S., Pflamm-Altenburg J., Kroupa P., 2012, MNRAS, 423, 1109
Pouliasis E., Matteo P. D., Haywood M., 2017, A&A, 598, 66
Retana-Montenegro E., van Hese E., Gentile G., Baes M., Frutos-Alfaro F., 2012, A&A, 540, 70

Robles V. H., Bullock J. S., 2021, MNRAS, 503, 5232
Rocha M., Peter A. H. G., Bullock J., 2012, MNRAS, 425, 231
Roederer I. U., Pace A. B., Placco V. M., Caldwell N., Koposov S. E., Mateo M., Olszewski E. W., Walker M. G., 2023, ApJ, 954, L55
Sauvaget T., Hammer F., Puech M., Yang Y. B., Flores H., Rodrigues M., 2018, MNRAS, 473, 2521
Seo M., Ann H. B., 2023, MNRAS
Sestito F., et al., 2023, MNRAS, 525, 2875
Simon J. D., 2019, ARA&A, 57, 375
Sollima A., Baumgardt H., 2017, MNRAS, 471, 3668
Torrealba G., et al., 2019, MNRAS, 488, 2743
Torrealba G., Koposov S. E., Belokurov V., Irwin M., 2016, MNRAS, 459, 2370
van den Bosch F. C., Ogiya G., Hahn O., Burkert A., 2018, MNRAS, 474, 3043
Vasiliev E., Baumgardt H., 2021, MNRAS, 505, 5978
Vitral E., Boldrini P., 2022, A&A, 667, 112
Walker M. G., Mateo M., Olszewski E. W., Peñarrubia J., Evans N. W., Gilmore G., 2009, ApJ, 704, L1274
Waller F., et al., 2023, MNRAS, 519, 1349
Wang J., Hammer F., Yang Y., 2022, MNRAS, 510, 2242
Wang J., Hammer F., Yang Y., Ripepi V., Cioni M.-R. L., Puech M., Flores H., 2019, MNRAS, 486, 5907
Wang J., Hammer F., Yang Y., Pawlowski M., Mamon G., Wang H., 2023, MNRAS, submitted
Weinberg M. D., 1994, ApJ, 108, L1403
Weisz D. R., Dolphin A. E., Skillman E. D., Holtzman J., Gilbert K. M., Dalcanton J. J., Williams B. F., 2014, ApJ, 789, L147
Wolf J., Martinez G. D., Bullock J. S., Kaplinghat M., Geha M., Muñoz R. R., Simon J. D., Avedo F. F., 2010, MNRAS, 406, 1220
Yang Y., Hammer F., Fouquet S., Flores H., Puech M., Pawlowski M. S., Kroupa P., 2014, MNRAS, 442, 2419
Yang Y., Hammer F., Jiao Y., Pawlowski M. S., 2022a, MNRAS, 512, 4171
Yang Y., Ianjamasimanana R., Hammer F., Higgs C., Namumba B., Carignan C., Józsa G. I. G., McConnachie A. W., 2022b, A&A, 660, 11
Zhang S., Mackey D., Da Costa G. S., 2022, MNRAS, 513, 3136

## APPENDIX A: ABOUT THE INFALL TIME OF DWARF GALAXIES

Barmentloo & Cautun (2023) proposed a machine learning technique to calculate the infall time of most MW dwarfs. Fig. A1 compares their results for 25 dwarfs. This Appendix examines the robustness of their analysis, and compares it to results from cosmological simulations (Rocha et al. 2012). We make the following points.

(i) Barmentloo & Cautun find an infall epoch for Sgr (and other associated dwarfs, see green points) that is later than that of VPOS dwarfs, while the Sgr system has a much smaller energy (see Fig. A1). This contradicts their own claim, that is, quoting them, 'we expect that there is a strong correlation between satellite orbital energy and infall time'.

(ii) The infall time for most dwarfs would be similar to that of the GSE major merger event in the MW, while the orbital energy of the later event is five times smaller;

(iii) The use of non-independent input features (e.g. distance, radial and total velocity versus total energy and angular momentum) to derive the infall time may lead to unreliable results, because some of them show a flat profile versus the infall time, that is, which likely dilutes the predictions;

(iv) According to their fig. 4, their technique can only retrieve input infall times smaller than 3–4 Gyr, that is, only for dwarfs shown in the bottom-left part of Fig. A1;

(v) Their choice of host galaxy halos in the EAGLE simulation appears not representative of the MW past history, that is, the

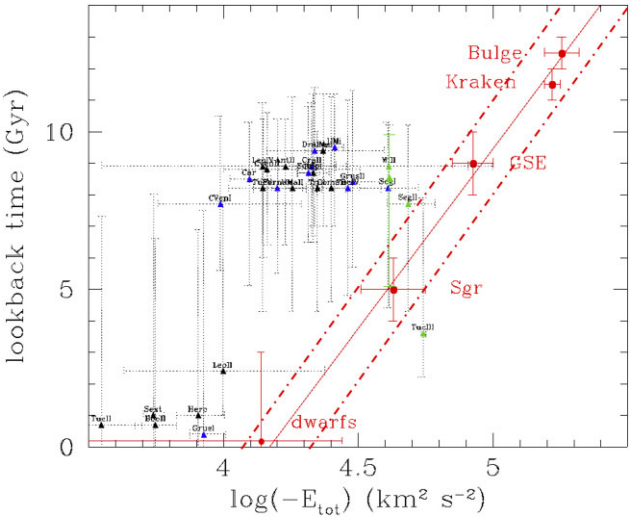


**Figure A1.** Comparison of the infall lookback time as a function of the orbital energy from Paper I, *red dots* and *line* joining MW merger events, which matches very well Rocha et al. (2012), the *two red dot-dashed lines* representing $\pm 1\,\sigma$. Besides this analysis based on a strong correlation between satellite orbital energy and infall time, *triangles* represent individual dwarfs infall times based on the method of Barmentloo & Cautun (2023, see text), showing how these predictions are discrepant from the expected relation with total orbital energy. The dwarfs associated with the VPOS and with Sgr are shown in *blue* and *green*, respectively.

significant increase of both pericentre and apocentre from 9 to 1 Gyr ago (see their fig. 1) requires considerable mass gains, while MW is known to have experienced its last major merger 9–10 Gyr ago, as shown from the analysis of the GSE event (Naidu et al. 2021);

Additionally, the choice of Barmentloo & Cautun (2023) to define the infall time as being the first time the future satellite is passing through the virial radius of the host lead to very scattered results according to Rocha et al. (2012). Consequently, predictions for infall times are better predicted through their tight correlation with orbital energy (Rocha et al. 2012), the latter being calculated with good accuracy from *Gaia* DR3 (see Paper I).

We also noticed the study by Pagnini et al. (2022), which may cast some doubts about the reliability of associating GCs to past merger events in the MW (Kruijssen et al. 2019, 2020; Malhan et al. 2022). However, this might be due to the following assumptions (1) that GCs originate in halos of infalling dwarfs and are not formed during merger events (e.g. Kraken GSE, or Pontus) that likely induced strong star formation events 12–9 Gyr ago (Haywood et al. 2016), (2) that all mergers experienced by the MW, including GSE, were minor (e.g. mass ratio of 1:10), contrary to the analysis by Naidu et al. (2021) who considered mass ratio from 1:2 to 1:4[17], and (3) that simulations without gas can reproduce the infall of stellar systems at epochs when the gas is preponderant. It is unlikely that all GCs have been formed through the way proposed by Pagnini et al. (2022). However, the latter study provides a complementary channel for explaining several GCs that are not identified inside a structure in the plane made by total energy and angular momentum (see fig. 5 of Paper I).

[17]Notice that these higher mass ratios are necessary to explain the origin of both thin and thick disc of a spiral galaxy like the MW (Hammer et al. 2009; Hopkins et al. 2010; Sauvaget et al. 2018; Hammer et al. 2018a).

**Table B1.** Structural properties of MW dwarfs including kinematics.

| Name | $L_V$ ($L_{sun}$) | $M_{stars}/L_V$ | $R_{GC}$ (kpc) | $r_{half}$ (pc) | $\epsilon$ | $\sigma_{los}$ (km s$^{-1}$) | $\sigma_{stars}$ (km s$^{-1}$) |
|---|---|---|---|---|---|---|---|
| Antlia II | $214\,783 \pm 29,600$ | 2.5 | $130.35^{+6.5}_{-6.5}$ | $2867^{+312}_{-312}$ | 0.38 | $5.71^{+1.08}_{-1.08}$ | $0.317 \pm 0.039$ |
| Aquarius II | $4742 \pm 613.2$ | 2.5 | $105.40^{+3.3}_{-3.3}$ | $160^{+26}_{-26}$ | 0.39 | $4.7^{+1.8}_{-1.2}$ | $0.2 \pm 0.029$ |
| Bootes I | $21\,880 \pm 5082$ | 2.5 | $63.64^{+2}_{-2}$ | $191^{+8}_{-8}$ | 0.30 | $5.1^{+0.6}_{-0.7}$ | $0.392 \pm 0.054$ |
| Bootes II | $1282 \pm 955$ | 2.5 | $39.82^{+1}_{-1}$ | $39^{+5}_{-5}$ | 0.25 | $2.9^{+1.6}_{-1.2}$ | $0.210 \pm 0.092$ |
| CanesVenatici I | $265\,500 \pm 14\,680$ | 2.5 | $210.8^{+6}_{-6}$ | $437^{+18}_{-18}$ | 0.44 | $7.6^{+0.4}_{-0.4}$ | $0.90 \pm 0.043$ |
| CanesVenatici II | $10\,000 \pm 2990$ | 2.5 | $160.6^{+4}_{-4}$ | $71^{+11}_{-11}$ | 0.40 | $4.6^{+1}_{-1}$ | $0.435 \pm 0.098$ |
| Carina | $515\,200 \pm 23\,740$ | 2.5 | $107.6^{+5}_{-5}$ | $311^{+15}_{-15}$ | 0.36 | $6.6^{+1.2}_{-1.2}$ | $1.49 \pm 0.070$ |
| ComaBerenices | $4406 \pm 1023$ | 2.5 | $43.19^{+1.55}_{-1.55}$ | $69^{+4.5}_{-4.5}$ | 0.37 | $4.6^{+0.8}_{-0.8}$ | $0.29 \pm 0.0435$ |
| Crater II | $162\,900 \pm 15\,030$ | 2.5 | $116.4^{+1.1}_{-1.1}$ | $1066^{+86}_{-86}$ | 0 | $2.7^{+0.3}_{-0.3}$ | $0.453 \pm 0.039$ |
| Draco | $304\,800 \pm 14\,040$ | 2.5 | $81.98^{+6}_{-6}$ | $231^{+17}_{-17}$ | 0.29 | $9.1^{+1.2}_{-1.2}$ | $1.331 \pm 0.079$ |
| Fornax | $18\,540\,000 \pm 2\,397\,000$ | 1.5 | $141^{+3}_{-3}$ | $792^{+18}_{-18}$ | 0.29 | $11.7^{+0.9}_{-0.9}$ | $4.34 \pm 0.330$ |
| Grus I | $3732 \pm 1192$ | 2.5 | $116.2^{+11.5}_{-11.5}$ | $28^{+23}_{-23}$ | 0.44 | $2.9^{+2.1}_{-1}$ | $0.423 \pm 0.241$ |
| Hercules | $18\,370 \pm 28867$ | 2.5 | $126.4^{+6}_{-6}$ | $216^{+20}_{-20}$ | 0.69 | $5.1^{+0.9}_{-0.9}$ | $0.338 \pm 0.042$ |
| Leo I | $4\,406\,000 \pm 1\,149\,000$ | 1.5 | $257.8^{+15.5}_{-15.5}$ | $270^{+16.5}_{-16.5}$ | 0.30 | $9.2^{+0.4}_{-0.4}$ | $3.62 \pm 0.58$ |
| Leo II | $673\,000 \pm 24\,800$ | 2.5 | $235.5^{+14}_{-14}$ | $171^{+10}_{-10}$ | 0.07 | $7.4^{+0.4}_{-0.4}$ | $2.3 \pm 0.10$ |
| Leo IV | $8472^{\pm}2048$ | 2.5 | $154.6^{+5}_{-5}$ | $114^{+13}_{-13}$ | 0.17 | $3.3^{+1.7}_{-1.7}$ | $0.316 \pm 0.056$ |
| Leo V | $4446 \pm 1501$ | 2.5 | $169.8^{+4}_{-4}$ | $49^{+16}_{-16}$ | 0.43 | $2.3^{+3.2}_{-1.6}$ | $0.349 \pm 0.115$ |
| Pegasus IV | $4800 \pm 800$ | 2.5 | $89^{+6}_{-6}$ | $41^{+8}_{-8}$ | 0.20 | $3.3^{+1.7}_{-1.1}$ | $0.396 \pm 0.071$ |
| Sculptor | $1\,820\,000 \pm 235\,300$ | 2.5 | $86.09^{+5}_{-5}$ | $279^{+16}_{-16}$ | 0.33 | $9.2^{+1.1}_{-1.1}$ | $2.96 \pm 0.27$ |
| Segue 1 | $283 \pm 205$ | 2.5 | $27.84^{+2}_{-2}$ | $24^{+4}_{-4}$ | 0.33 | $3.7^{+1.4}_{-1.1}$ | $0.1259 \pm 0.056$ |
| Sextans | $322\,100 \pm 17\,810$ | 2.5 | $97.97^{+3}_{-3}$ | $456^{+15}_{-15}$ | 0.30 | $7.9^{+1.3}_{-1.3}$ | $0.97 \pm 0.042$ |
| Tucana II | $3105 \pm 575$ | 2.5 | $54.24^{+8}_{-8}$ | $121^{+35}_{-35}$ | 0.39 | $8.6^{+4.4}_{-2.7}$ | $0.185 \pm 0.044$ |
| UrsaMajor I | $9638 \pm 3443$ | 2.5 | $101.9^{+5.85}_{-5.85}$ | $295^{+28}_{-28}$ | 0.59 | $7^{+1}_{-1}$ | $0.2095 \pm 0.047$ |
| UrsaMajor II | $5058 \pm 1223$ | 2.5 | $40.81^{+1.95}_{-1.95}$ | $139^{+9}_{-9}$ | 0.56 | $5.6^{+1.4}_{-1.4}$ | $0.221 \pm 0.033$ |
| UrsaMinor | $349\,900^{\pm}16,120$ | 2.5 | $77.89^{+4}_{-4}$ | $405^{+21}_{-21}$ | 0.55 | $9.5^{+1.2}_{-1.2}$ | $1.0776 \pm 0.0527$ |
| Willman 1 | $1236 \pm 909$ | 2.5 | $49.62^{+10}_{-10}$ | $33^{+8}_{-8}$ | 0.47 | $4^{+0.8}_{-0.8}$ | $0.224 \pm 0.109$ |

## APPENDIX B: INTRINSIC PARAMETERS OF MW DWARF GALAXIES

Table B1 describes the structural parameters of the MW dwarf galaxies. Column 1: dwarf galaxy name; Column 2: V-luminosity; Column 3: stellar mass to light ratio; Column 4: Galactocentric distance; Column 5: half-light radius or effective radius; Column 6: dwarf ellipticity; Column 7: line-of-sight velocity dispersion; Column 8: velocity dispersion due to the sole stellar component.

Data of Table B1 are taken from the review by Simon (2019, see also references therein), and have been updated by more recent measurements. The latter include:

(i) New estimates of $\sigma_{los}$ for Bootes I, Leo IV, and LeoV (Jenkins et al. 2021);

(ii) Last update by Josh Simon of Simon (2019) with a new value for $\sigma_{los}$ of Grus I, and Leo V;

(iii) New measurements from Bruce et al. (2023) of $\sigma_{los}$ for Aquarius II (8 spectroscopic stars, 4.7 instead of 5.4) and Bootes II (2.9 instead of 8.2!);

(iv) First robust measurements of $\sigma_{los}$ of Pegasus IV (Cerny et al. 2023);

(v) Data for both Antlia II and Crater II (Torrealba et al. 2016; Caldwell et al. 2017; Torrealba et al. 2019; Ji et al. 2021).

The sample of dwarf galaxies comes from table 1 of Li et al. (2021) for 46 dwarfs. Here, we only include objects within 300 kpc (excluding Eridanus II), and for which a measurement of $\sigma_{los}$ has been performed without ambiguity. The latter condition leads to remove 5 dwarf galaxies having less than 5 stars with both *Gaia* and spectroscopy data. It would lead to 40 dwarfs, to which we have further removed the 3 potential GCs (Crater, Draco II, and Sgr II), and 5 dwarfs (Carina II, Carina III, Phoenix II, Horologium I, Hydrus I, and Reticulum II) associated to the LMC. Also associated to the LMC, Carina III is already excluded since only 4 of its stars possess spectroscopy. Similarly, Columba I (3), Horologium II (1), Pisces II (3), and Reticulum III (3) are not considered due to their lack of spectroscopic stars (which numbers are given in parenthesis). Finally, we have also removed Grus II, Hydra II, Segue 2, Triangulum II, Tucana III, Tucana IV, and Tucana V, because only a limit on their velocity dispersion can be determined (Simon 2019, see also references therein).

However, in this paper, we have reintegrated Aquarius II (8 spectroscopic stars) and Pegasus IV, since for both galaxies their velocity dispersion has been measured. It leaves us with a sample of 26 galaxies, all with more than 10 spectroscopic stars, except for Aquarius II, Grus I, Leo IV, Leo V, Pegasus IV, Ursa Major II, and Willman.

**Table B2.** Dwarf eccentricities for the four MW DM mass models of Table 1. The seven dwarfs without estimates of their internal velocity dispersions have their names in italics.

| Dwarf | $\text{Einasto}_{\text{HM}}$ | NFW | $\text{Einasto}_{\text{MM}}$ | $\text{Einasto}_{\text{LM}}$ |
|---|---|---|---|---|
| AntliaII | 0.454 | 0.414 | 0.494 | 1.08 |
| AquariusII | 0.312 | 0.581 | 1.31 | 3.001 |
| BootesI | 0.333 | 0.444 | 0.649 | 1.55 |
| BootesII | 0.641 | 0.91 | 1.803 | 2.968 |
| CanesVenaticiI | 0.599 | 0.659 | 0.829 | 1.301 |
| CanesVenaticiII | 0.728 | 0.765 | 0.875 | 0.998 |
| Carina | 0.076 | 0.303 | 0.871 | 2.347 |
| ComaBerenices | 0.323 | 0.471 | 0.656 | 1.549 |
| CraterII | 0.603 | 0.584 | 0.598 | 0.764 |
| Draco | 0.413 | 0.456 | 0.573 | 1.217 |
| Fornax | 0.361 | 0.262 | 0.325 | 1.099 |
| GrusI | 0.821 | 0.913 | 1.446 | 1.795 |
| *GrusII* | 0.478 | 0.538 | 0.594 | 0.884 |
| Hercules | 0.608 | 0.763 | 1.231 | 2.196 |
| *HydraII* | 1.874 | 3.614 | 5.912 | 11.23 |
| LeoI | 0.9 | 1.539 | 1.885 | 3.056 |
| LeoII | 0.512 | 0.474 | 0.607 | 0.954 |
| LeoIV | 0.594 | 0.745 | 0.899 | 1.268 |
| LeoV | 0.967 | 2.438 | 4.469 | 8.846 |
| PegasusIV | 0.52 | 0.476 | 0.448 | 0.455 |
| Sculptor | 0.323 | 0.365 | 0.518 | 1.308 |
| Segue1 | 0.475 | 0.525 | 0.572 | 0.821 |
| *Segue2* | 0.416 | 0.404 | 0.398 | 0.399 |
| Sextans | 0.385 | 0.752 | 1.614 | 3.375 |
| *TriangulumII* | 0.802 | 0.861 | 0.935 | 1.732 |
| TucanaII | 0.682 | 0.955 | 1.872 | 2.982 |
| *TucanaIII* | 0.873 | 0.881 | 0.886 | 0.91 |
| *TucanaIV* | 0.357 | 0.429 | 0.521 | 1.07 |
| *TucanaV* | 0.609 | 0.765 | 1.336 | 2.278 |
| UrsaMajorI | 0.318 | 0.247 | 0.272 | 0.565 |
| UrsaMajorII | 0.476 | 0.649 | 0.927 | 2.056 |
| UrsaMinor | 0.372 | 0.372 | 0.43 | 0.857 |
| Willman | 0.249 | 0.247 | 0.265 | 0.332 |

## APPENDIX C: PROPERTIES OF PERICENTRE VELOCITY

Fig. C1 shows that for GCs, $V_{\text{peri}}$ is rather constant (logarithmic slope −0.16) with large variations of $R_{\text{peri}}$

$$V_{\text{peri}} = V_{\text{peri}} = 398\,\text{km}\,\text{s}^{-1}\,\text{R}_{\text{peri}}^{-0.16} \tag{C1}$$

The slope is slightly steeper for dwarfs (–0.2), which also show a stronger correlation ($\rho = 0.9$) than GCs.

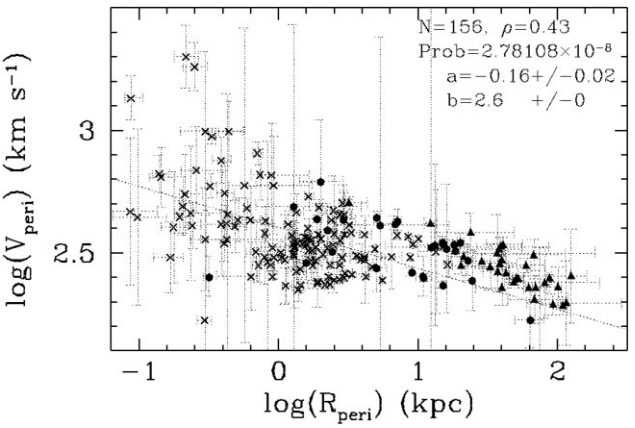


**Figure C1.** $V_{\text{peri}}$ versus $R_{\text{peri}}$ in logarithmic scale for HSB-GCs (*crosses*), LSB-GCs (*full dots*), and dwarfs (*triangles*). The *dotted* line indicates the best fit of the correlation for 156 GCs (see parameters on the top-right).

This paper has been typeset from a TEX/LATEX file prepared by the author.